

LEADER: Lightweight End-to-End Attention-Gated Dual Autoencoder for Robust Minutiae Extraction

Raffaele Cappelli and Matteo Ferrara

Abstract—Minutiae extraction, a fundamental stage in fingerprint recognition, is increasingly shifting toward deep learning. However, truly end-to-end methods that eliminate separate preprocessing and postprocessing steps remain scarce. This paper introduces LEADER (Lightweight End-to-end Attention-gated Dual autoencodER), a neural network that maps raw fingerprint images to minutiae descriptors, including location, direction, and type. The proposed architecture integrates non-maximum suppression and angular decoding to enable complete end-to-end inference using only 0.9 M parameters. It employs a novel “Castle-Moat-Rampart” ground-truth encoding and a dual-autoencoder structure, interconnected through an attention-gating mechanism. Experimental evaluations demonstrate state-of-the-art accuracy on plain fingerprints and robust cross-domain generalization to latent impressions. Specifically, LEADER attains a 34% higher F_1 -score on the NIST SD27 dataset compared to specialized latent minutiae extractors. Sample-level analysis on this challenging benchmark reveals an average rank of 2.07 among all compared methods, with LEADER securing the first-place position in 47% of the samples—more than doubling the frequency of the second-best extractor. The internal representations learned by the model align with established fingerprint domain features, such as segmentation masks, orientation fields, frequency maps, and skeletons. Inference requires 15 ms on GPU and 322 ms on CPU, outperforming leading commercial software in computational efficiency. The source code and pre-trained weights are publicly released to facilitate reproducibility.

Index Terms—Biometrics, Convolutional neural networks, End-to-end learning, Attention mechanisms, Interpretability, Generalization, Fingerprint recognition, Automatic minutiae detection, Latent fingerprints, Open source software.

I. INTRODUCTION

BIOMETRIC recognition is a cornerstone of modern identity management, with fingerprint identification remaining one of the most widely adopted modalities due to its permanence, uniqueness, and high discriminative power [1]. At the core of automated fingerprint identification systems (AFIS) lies minutiae extraction, specifically the detection of ridge endings and bifurcations (Fig. 1a). The spatial distribution, type, and direction of these local features form the basis for high-security fingerprint comparison. However, robust and precise minutiae extraction remains challenging, particularly for latent impressions or low-quality images [2].

Historically, minutiae extraction relied on multi-stage pipelines involving image enhancement, binarization, and morphological thinning to produce a one-pixel-wide skeleton map [1]. Although effective on high-quality fingerprints, these

The authors are with the Department of Computer Science and Engineering of the University of Bologna, Italy (e-mail: raffaele.cappelli@unibo.it, matteo.ferrara@unibo.it).

The `pyfing` package, including source code and pre-trained weights for LEADER, is available at <https://github.com/raffaele-cappelli/pyfing>.

traditional methods are prone to false detections and omissions when ridge patterns are degraded. To address these limitations, the field has shifted toward deep learning-based approaches. Early neural methods used sliding-window classifiers or patch-based analysis, which are computationally expensive and often lack global context. More recently, fully convolutional architectures have enabled the processing of entire images in a single forward pass.

Despite these advances, state-of-the-art (SOTA) models still require external preprocessing or significant post-inference operations, as summarized in Table I. Moreover, many recent architectures require large parameter counts to maintain accuracy, limiting their suitability for resource-constrained devices.

In this paper, we propose LEADER (Lightweight End-to-end Attention-gated Dual autoencodER), a fully convolutional model designed to map raw fingerprint images directly to comprehensive minutiae attributes: location, direction, type, and quality score. This unified approach eliminates handcrafted preprocessing and off-graph postprocessing, while delivering top-tier accuracy with remarkable parameter efficiency.

The main contributions of this work are as follows.

- 1) A *fully end-to-end framework* that integrates the entire extraction process—including non-maximum suppression (NMS)—into the network, enabling direct readout of complete minutiae attributes.
- 2) An *adaptive ground-truth encoding*, termed Castle-Moat-Rampart (CMR), which uses spatially modulated weighting to disambiguate adjacent minutiae and improve localization robustness against labeling jitter.
- 3) A *lightweight model* with two autoencoders and a specialized attention gate, achieving high-accuracy minutiae extraction with 0.9 M parameters.
- 4) A *modernized convolutional backbone* incorporating separable convolutions, inverse bottlenecks, dilated kernels, and mixed pooling, optimized for accuracy and efficiency [3].
- 5) *Cross-domain generalization to latent fingerprints* despite training exclusively on non-latent samples, with performance exceeding existing SOTA methods and commercial off-the-shelf (COTS) systems.
- 6) An *interpretability study*, showing that LEADER autonomously learns features aligned with traditional fingerprint concepts—such as segmentation masks, orientation fields, frequency maps, and ridge and valley skeletons—without explicit supervision.
- 7) An *integrated open-source package* (`pyfing`), including pre-trained weights for immediate reproducibility and further research.

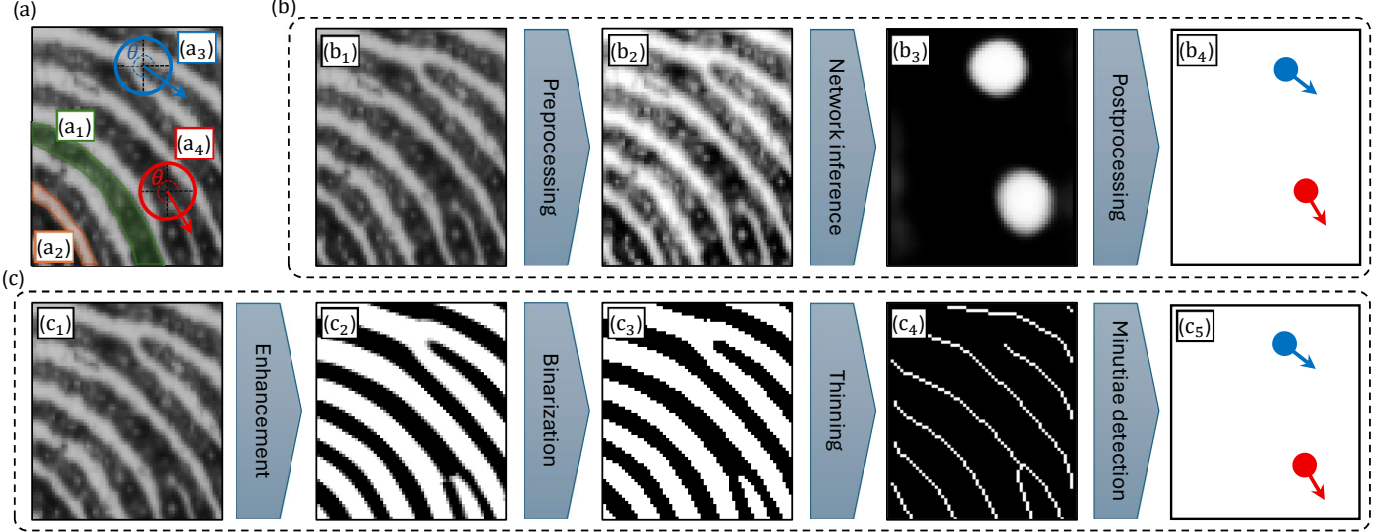


Fig. 1. **Overview of fingerprint patterns and extraction paradigms.** (a) Local ridge structure highlighting a ridge (a₁), a valley (a₂), a ridge ending (a₃), and a bifurcation (a₄), with their corresponding directions θ . (b) Conventional deep learning-based pipeline: the input image (b₁) is typically preprocessed (b₂) and fed into a neural network to generate heatmaps (b₃), requiring off-graph postprocessing to obtain the final minutiae (b₄). (c) Traditional extraction workflow: the input image (c₁) is enhanced (c₂), binarized (c₃), and thinned to a ridge skeleton (c₄) before connectivity analysis yields the minutiae (c₅).

The remainder of this paper is organized as follows. Section II reviews the evolution of minutiae extraction methods. Section III describes the proposed LEADER architecture, detailing its cascaded feature extraction, on-graph postprocessing, ground-truth encoding, and multi-task optimization. Section IV presents experimental evaluations, comparative analyses, ablation studies, and interpretability investigations. Section V summarizes the contributions and outlines future directions. Supplementary Material (Appendices A–D) provides technical notation, architectural specifications, implementation details, training dynamics, and extended sample-level performance analyses, including aggregate ranking statistics and visual comparisons of extraction accuracy.

II. RELATED WORKS

Minutiae extraction has evolved from handcrafted morphological pipelines toward sophisticated deep learning architectures. This section reviews the milestones of this progression, from foundational methods to the latest neural approaches.

A. Traditional Methods

Earlier solutions are generally categorized into binarization-based frameworks and direct gray-scale approaches.

1) *Binariation-based Extraction*: These classic frameworks rely on a multi-stage sequential process (Fig. 1c). The workflow begins with image enhancement and ridge-valley binarization, followed by morphological thinning to generate a one-pixel-wide skeleton [1]. Minutiae are then detected by analyzing local pixel connectivity, typically through the *crossing number* technique, which identifies ridge endings and bifurcations by counting ridge-to-valley transitions in a 3×3 neighborhood [1]. Although effective for high-quality fingerprints, this pipeline is notably vulnerable to noise. To mitigate artifacts such as “hairy” skeletons or spurs, regularization via morphological operators or adaptive filtering is

often employed. However, these measures frequently fail to eliminate spurious minutiae, necessitating additional heuristic postprocessing that increases computational complexity.

2) *Direct Gray-scale Extraction*: Several methods operate directly on gray-scale intensities to mitigate the information loss and artifacts typical of binarization and thinning. These approaches generally follow one of two strategies. The first is *ridge following*, exemplified by the algorithm in [4], which tracks ridges along the orientation field to detect intensity maxima on orthogonal cross-sections. While this avoids binarization errors, the sequential nature of the process requires precise tuning and lacks robustness in low-quality areas. The second strategy, *singularity modeling*, treats minutiae as local discontinuities in the ridge flow. Techniques based on parabolic symmetries [5] or frequency modulation [6] provide rigorous frameworks but often exhibit lower precision than modern learning-based alternatives.

B. Deep Learning-based Methods

Recent advancements have established deep learning as the dominant paradigm. Table I provides a taxonomy of representative methods, tracing the evolution from local classifiers to integrated pipelines.

1) *Patch-based Classifiers*: Early neural approaches [7]–[9] employ sliding-window strategies to classify individual patches as minutia or non-minutia. This binary output space precludes the inference of direction and type, while the overlapping scans result in high computational redundancy and lack of global context.

2) *Two-stage and Multi-pass Frameworks*: To incorporate broader context while maintaining precision, certain architectures adopt a multi-stage design. Methods in [10], [12], [14] utilize an initial convolutional neural network (CNN) to identify candidate regions, followed by refinement (e.g., ROI-pooling or patch analysis) to regress coordinates and

TABLE I
EVOLUTION OF DEEP LEARNING-BASED MINUTIAE EXTRACTION METHODS AND COMPARISON WITH LEADER.

Method	Single-pass	End-to-end	Minutiae direction	Minutiae type	Parameters (M)	Open-source
Sankaran <i>et al.</i> (2014) [7]	No ¹	No	No	No	29.7	No
Jiang <i>et al.</i> (2016) [8]	No ¹	No	No	No	11.2	No
Darlow and Rosman (2017) [9]	No ¹	No	No	No	3.3	No
Tang, Gao and Feng (2017) [10]	No ²	No	Yes	No	108.3	No
Tang <i>et al.</i> (2017) [11]	Yes	No ⁴	Yes	No	4.7	Yes
Nguyen, Cao, and Jain (2018) [12]	No ²	No	Yes	No	74.4	Yes
Nguyen <i>et al.</i> (2020) [13]	Yes	No ⁴	Yes	No	7.0	No
Zhou <i>et al.</i> (2020) [14]	No ²	No	Yes	No	70.4	No
Cao <i>et al.</i> (2020) [15]	No ³	No	Yes	No	5.5	Yes
Zhang, Liu, and Liu (2021) [16]	Yes	No ⁴	Yes	No	36.5	No
Feng and Kumar (2023) [17]	Yes	No ⁴	Yes	No	2.2	No
LEADER (Ours)	Yes	Yes	Yes	Yes	0.9	Yes

¹ Sliding-window inference: requires multiple passes over local sub-regions.

² Two-stage pipeline: initial localization followed by region-specific refinement (e.g., ROI pooling or patch analysis).

³ Multi-pass inference: five separate forward passes on externally enhanced inputs.

⁴ Off-graph processing (e.g., post-inference NMS or angular decoding of minutiae directions).

directions. Other approaches, such as [15], perform multi-pass inference on externally enhanced inputs. Although more accurate than patch-based classifiers, these frameworks are computationally intensive due to their iterative execution and high parameter counts.

3) *Single-pass Pipelines*: The current state of the art involves CNNs designed for single-pass inference [11], [13], [16], [17]. These models process the entire fingerprint in a single forward pass (Fig. 1b) to produce feature maps from which minutiae are derived. FingerNet [11] pioneered this shift by embedding traditional processing steps within differentiable layers. Despite their improved efficiency, these methods lack a fully end-to-end architecture due to off-graph dependencies (e.g., external NMS) and typically provide incomplete attribute extraction by omitting minutiae type. The proposed LEADER architecture addresses these gaps by internalizing the entire pipeline within a single on-graph computational flow, enabling the joint extraction of position, direction, and type.

III. THE LEADER ARCHITECTURE

The proposed architecture is built upon four constituent elements: (i) cascaded feature extraction employing two autoencoders with skip connections and attention-gating (Sec. III-A); (ii) integrated postprocessing through on-graph NMS and trigonometric decoding (Sec. III-B); (iii) adaptive ground-truth encoding for high-precision localization (Sec. III-C); and (iv) multi-task optimization for synchronized attribute learning (Sec. III-D). For reference, the mathematical notation used throughout this work is provided in Appendix A (Supplementary Material).

A. Cascaded Feature Extraction

The internal structure of LEADER comprises five components (Fig. 2). The extraction process follows a cascaded refinement paradigm designed to balance spatial precision with semantic depth. Detailed diagrams of each component and their constituent functional blocks are provided in the Supplementary Material (Figs. 12–16).

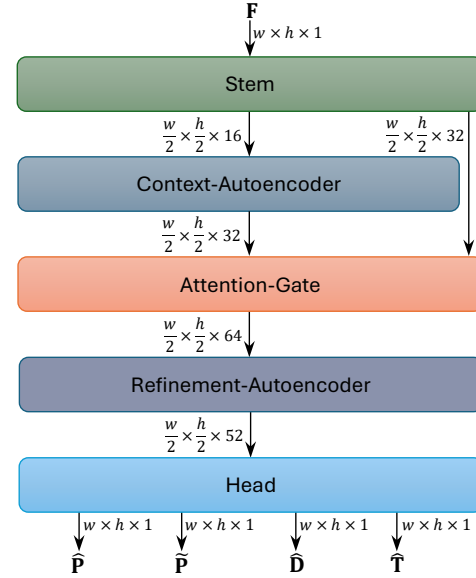


Fig. 2. **High-level diagram of the LEADER model.** The network processes the fingerprint \mathbf{F} through a pipeline composed of the *Stem*, the *Context-Autoencoder*, the *Attention-Gate*, the *Refinement-Autoencoder*, and the multi-task *Head* producing position ($\hat{\mathbf{P}}$), direction ($\hat{\mathbf{D}}$), and type ($\hat{\mathbf{T}}$) maps.

1) *Stem*: This component performs initial feature extraction and spatial mapping, accepting the fingerprint $\mathbf{F} \in \mathbb{R}^{w \times h \times 1}$ as input.¹ The *Stem* adopts a dual-path configuration (Fig. 12) comprising two *StemBlocks* with distinct pooling strategies. Each *StemBlock* (Fig. 16d) is designed to capture local ridge details and wider contextual patterns.

2) *Context-Autoencoder*: This stage extracts mid-level topological features through a symmetric skip-autoencoder (Fig. 15). The encoding path employs *SeparableConvBlocks* (Fig. 16c) for computationally efficient feature extraction, while spatial resolution is progressively reduced through *DownsamplingBlocks* (Fig. 16a) to attenuate noise and expand

¹To ensure compatibility with downsampling layers, \mathbf{F} is padded to dimensions that are multiples of 32 pixels, using the intensity of the top-left pixel as a constant background value.

the effective receptive field. Symmetrically, the decoding path restores the original spatial resolution using *UpsamplingBlocks* (Fig. 16b). Feature maps from the encoder are transferred to the decoder through channel-wise concatenation (skip connections), ensuring the preservation of fine-grained structural details alongside high-level representations.

3) *Attention-Gate*: To prioritize salient ridge structures for the subsequent refinement stage, this component performs multi-scale spatial and channel-wise recalibration of the feature maps \mathbf{X} generated by the *Context-Autoencoder*. The gating mechanism (Fig. 13) captures contextual information across varying receptive-field sizes through three parallel convolutional paths with different dilation rates. Formally, the gating signal \mathbf{X}_{gate} is defined as $\mathbf{X}_{gate} = \varsigma(\psi([\Delta_1(\mathbf{X}), \Delta_3(\mathbf{X}), \Delta_6(\mathbf{X})]))$, where $[\cdot]$ denotes channel-wise concatenation, Δ_r represents a 3×3 convolution with 16 filters and dilation rate $r \in \{1, 3, 6\}$ followed by a GELU activation, ψ is a point-wise convolution that reduces the channel depth to 32, and ς is the Sigmoid activation function. The refined feature maps \mathbf{X}' are obtained by modulating the original features \mathbf{X} through element-wise multiplication with the gating signal, $\mathbf{X}' = \mathbf{X} \odot \mathbf{X}_{gate}$. These are subsequently concatenated with high-resolution feature maps received through a direct skip connection from the *Stem* (Fig. 2). This design ensures that the final refinement stage operates on a saliency-calibrated representation spatially aligned to the original ridge geometry.

4) *Refinement-Autoencoder*: This stage (Fig. 15) performs high-level semantic refinement by substituting the separable convolutions of the *Context-Autoencoder* with *InvBottleneckConvBlocks* (Fig. 16f). These blocks employ an expansion-contraction pattern, projecting features into a higher-dimensional space through point-wise convolutions before compressing them to the original depth. This design facilitates complex representation learning while maintaining high parameter efficiency. Furthermore, this autoencoder employs a non-monotonic channel distribution to enforce a strategic bottleneck for topological encoding. After reaching a peak depth of 128 channels, the architecture undergoes a sharp contraction to 32 channels at the fourth *InvBottleneckConvBlock*, reaching its dimensional minimum of 27 channels in the subsequent block. This localized compression at the transition between the contracting and expanding paths is designed to filter redundant information while preserving essential topological features. The remainder of the decoder is optimized with precisely tuned channel dimensions to maintain representational capacity and an overall footprint of 0.9 M parameters.

5) *Head*: This component transforms the feature maps generated by the *Refinement-Autoencoder* into the final minutiae attributes. Its structure (Fig. 14) branches into three parallel *HeadBlocks* (Fig. 16e), each employing an *InvBottleneckConvBlock* with six filters. The *Head* decodes the 52 input feature maps into task-specific projections through specialized output layers, using Sigmoid activations for the position and type maps ($\hat{\mathbf{P}}, \hat{\mathbf{T}}$), and linear regression for the direction map $\hat{\mathbf{D}}$ to maintain its dynamic range.

B. Integrated Postprocessing

LEADER internalizes the extraction logic typically performed by off-graph heuristics, producing four synchronized output maps directly within the computational flow.

1) *On-graph NMS*: A specific layer (Fig. 14, Supplementary Material) replaces external peak-finding algorithms. The predicted position map $\hat{\mathbf{P}}$ is smoothed with a 5×5 Gaussian kernel to yield $\hat{\mathbf{P}}^*$. The refined map $\tilde{\mathbf{P}}$ is then generated through local spatial competition:

$$\tilde{p}_{ij} = \begin{cases} \hat{p}_{ij}^* & \text{if } \hat{p}_{ij}^* = \max_{(x,y) \in \mathcal{N}_7(j,i)} \hat{p}_{yx}^* \\ 0 & \text{otherwise} \end{cases} \quad (1)$$

where $\mathcal{N}_7(j, i)$ denotes a 7×7 spatial neighborhood centered at (j, i) . This operation is implemented through unit-stride MaxPooling2D followed by element-wise comparison.

2) *Trigonometric Directional Decoding*: To account for the circular nature of minutiae directions while maintaining optimization stability, the network regresses two Cartesian component maps, $(\hat{\mathbf{V}}_x, \hat{\mathbf{V}}_y)$, rather than a single angular representation. This approach maps the targets into a continuous Euclidean space, avoiding the discontinuities and instability inherent in periodic angular regression. The final direction map $\hat{\mathbf{D}}$ is subsequently recovered on-graph by the *CartesianToPolar* layer (Fig. 14, Supplementary Material) using the element-wise differentiable *arctan2* operator: $\hat{\mathbf{D}} = \text{arctan2}(\hat{\mathbf{V}}_y, \hat{\mathbf{V}}_x)$.

3) *Minutiae List Extraction*: The dense output maps are converted into a sparse minutiae set $\hat{\mathbb{M}}$ through a thresholding pass. For every pixel where $\tilde{p}_{ij} \geq \tau_q$, a minutia tuple $\hat{m}_k = (\hat{x}_k, \hat{y}_k, \hat{\theta}_k, \hat{t}_k, \hat{q}_k)$ is added to $\hat{\mathbb{M}}$, where:

- $(\hat{x}_k, \hat{y}_k) = (j, i)$ are the Cartesian coordinates;
- $\hat{\theta}_k = \hat{d}_{ij}$ is the predicted direction;
- \hat{t}_k is the type: ridge ending if $\hat{t}_{ij} \geq 0.5$, bifurcation otherwise;
- $\hat{q}_k = \tilde{p}_{ij}$ is a reliability value representing the quality score of \hat{m}_k .

C. Adaptive Ground-Truth Encoding

A critical challenge in training deep networks for minutiae extraction lies in the translation of discrete ground-truth annotations into continuous heatmaps suitable for multi-task learning. Direct regression of sparse attributes for each minutia $m_k = (x_k, y_k, \theta_k, t_k)$ is ill-posed due to extreme class imbalance and the spatial uncertainty of manual annotations [18].

Recent deep learning methods have increasingly prioritized this encoding step. Early approaches relied on coarse-grained heatmaps at $w/8 \times h/8$ resolution [11], whereas subsequent approaches adopted $w/4 \times h/4$ representations [14] and incorporated Gaussian kernels to produce smoother heatmaps [16]. More recently, a concentric-zone encoding strategy was introduced [17], defining positive and negative regions around each minutia separated by a neutral annular buffer; pixels within this transition zone are specifically excluded from the loss function to mitigate gradient ambiguity.

Building upon these concepts, LEADER introduces a more sophisticated encoding and weighting strategy designed to preserve localization precision in high-density regions. Unlike

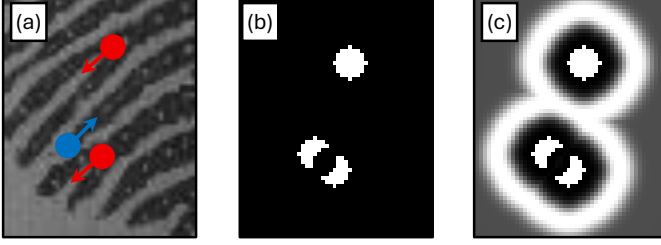


Fig. 3. **Ground-truth encoding and adaptive spatial weighting.** (a) Detail of a fingerprint image with annotated minutiae. (b) Generated binary position map \mathbf{P} : the morphology of the positive components is dynamically constrained in high-density regions to prevent spatial overlap. (c) Corresponding weight map \mathbf{W} , derived from the CMR geometry. The penalty zones adaptively reshape to maintain separation between closely spaced minutiae; the *castle* regions in \mathbf{W} correspond to positive pixels in \mathbf{P} , while the *ramparts* provide localized penalty peaks to enforce sharp localization.

static approaches, this method employs an adaptive formulation that dynamically reshapes target regions based on minutiae proximity. The binary ground-truth minutiae position map \mathbf{P} is defined as:

$$p_{ij} = \begin{cases} 1 & \text{if } \exists m_k \in \mathbb{M} : \rho(m_k, i, j) \leq \delta \\ & \text{and } \nexists m_k \in \mathbb{M} : \delta < \rho(m_k, i, j) \leq \delta + \beta \\ 0 & \text{otherwise} \end{cases} \quad (2)$$

where $\rho(m_k, i, j) = \sqrt{(j - x_k)^2 + (i - y_k)^2}$ denotes the Euclidean distance between minutia m_k and the pixel at Cartesian coordinates (j, i) . Under this definition, each connected component of pixels labeled as 1 is unambiguously associated with exactly one minutia. In regions of high minutiae density, this logic dynamically constrains the positive regions to ensure a separation of at least β pixels between neighboring features. This results in non-circular morphologies (e.g., those observed in Fig. 3b), which effectively prevent gradient interference during training.

To guide the optimization, a spatial weight map \mathbf{W} is derived, where each element is computed as $w_{ij} = \omega(\rho_{\min}(\mathbf{P}, i, j))$. Here, $\rho_{\min}(\mathbf{P}, i, j)$ represents the Euclidean distance to the nearest positive pixel in \mathbf{P} :

$$\rho_{\min}(\mathbf{P}, i, j) = \min_{(x, y) : p_{yx}=1} \sqrt{(j - x)^2 + (i - y)^2} \quad (3)$$

The weight map is modulated by a piece-wise function $\omega(s)$, designed to generate the CMR geometry (Fig. 4):

$$\omega(s) = \begin{cases} 1 & \text{if } s = 0 \\ 0 & \text{if } 0 < s \leq \beta \\ \mathcal{G}(s - s_1) & \text{if } \beta < s \leq s_1 \\ 1 & \text{if } s_1 < s \leq s_1 + \beta \\ \lambda + (1 - \lambda)\mathcal{G}(s - s_1 - \beta) & \text{otherwise} \end{cases} \quad (4)$$

where $s_1 = \beta + 3\sigma$ and $\mathcal{G}(z) = \exp(-z^2/2\sigma^2)$. As illustrated in Fig. 4, this weighting function yields a profile consisting of a positive core (*castle*), a zero-gradient uncertainty buffer (*moat*) to mitigate labeling jitter, and a localized penalty peak (*rampart*) that enforces sharp localization. This geometry ensures that the network prioritizes accurate placement by penalizing false activations in the immediate vicinity of each minutia

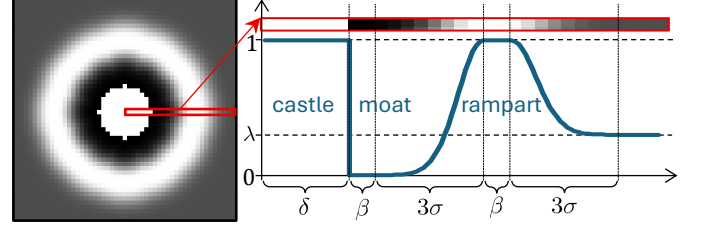


Fig. 4. **Radial profile of the CMR weighting strategy.** Left: 2D weight map \mathbf{W} for an isolated minutia. Right: Profile of the weighting function $\omega(\rho_{\min}(\cdot))$ along a cross-section from the center (pixels are highlighted in red). The *castle* ($w_{ij} = 1$) covers the central region—nominally of radius δ , but dynamically adjusted in high-density areas—followed by a zero-gradient *moat* of width β , which effectively extends into the lower tail of the Gaussian slope. The *rampart* rises to a peak penalty ($w_{ij} = 1$) to enforce sharp localization before descending to the background plateau λ .

before the weight descends to the background plateau λ . In high-density areas, the interaction of these adaptive profiles ensures that the network resolves closely spaced minutiae without interference (Fig. 3c).

Finally, the ground-truth direction map \mathbf{D} and type map \mathbf{T} are generated by assigning the attributes of the nearest minutia $m^* \in \mathbb{M}$ to each pixel (i, j) :

$$d_{ij} = \theta^*, \quad t_{ij} = t^*, \quad \text{where } m^* = \arg \min_{m_k \in \mathbb{M}} \rho(m_k, i, j) \quad (5)$$

where θ^* and t^* denote the direction and type of m^* , respectively. While these maps are defined globally for implementation convenience, they are subject to a conditional masking strategy during training; specifically, the loss terms for direction and type are restricted to pixels where $p_{ij} = 1$ to ensure that gradients are derived exclusively from valid minutiae locations (see Sec. III-D).

The CMR encoding is governed by four hyperparameters $(\delta, \beta, \sigma, \lambda)$, tuned for 500 DPI fingerprint sensors. Further details are provided in Appendix C (Supplementary Material).

D. Multi-task Optimization

LEADER is trained by means of a composite loss function $\mathcal{L} = \alpha_p \mathcal{L}_p + \alpha_d \mathcal{L}_d + \alpha_t \mathcal{L}_t$, where hyperparameters α_p , α_d , and α_t balance spatial localization, directional regression, and type classification, respectively. Each loss term (\mathcal{L}_p , \mathcal{L}_d , and \mathcal{L}_t) is computed by comparing the predicted maps ($\hat{\mathbf{P}}$, $\hat{\mathbf{D}}$, $\hat{\mathbf{T}}$) with their ground-truth counterparts (\mathbf{P} , \mathbf{D} , \mathbf{T}). Notably, the NMS-refined map $\tilde{\mathbf{P}}$ is excluded from optimization; as a deterministic transformation of $\hat{\mathbf{P}}$ through non-trainable layers, its role is to provide an integrated inference path rather than a supervisory target.

The position loss \mathcal{L}_p is defined as a weighted Binary Cross Entropy (BCE) modulated by the CMR weight map \mathbf{W} :

$$\mathcal{L}_p = \frac{\sum_{i,j} w_{ij} \cdot \text{BCE}(p_{ij}, \hat{p}_{ij})}{\sum_{i,j} w_{ij} + \epsilon} \quad (6)$$

This formulation ensures a strong supervisory signal at true minutiae locations (*castle*) and enforces sharp localization via the *rampart* penalty, while the zero-weight *moat* prevents ambiguous gradients from hindering the convergence in regions of high labeling uncertainty.

Secondary attributes are supervised through a conditional masking strategy. Since predicting direction or type at non-minutia locations is ill-posed, these pixels are excluded from the loss via \mathbf{P} . The directional loss \mathcal{L}_d is computed as the normalized masked Root Mean Square (RMS) of the angular difference $\phi(d_{ij}, \hat{d}_{ij}) = [(d_{ij} - \hat{d}_{ij} + \pi) \bmod 2\pi] - \pi$:

$$\mathcal{L}_d = \frac{1}{\pi} \sqrt{\frac{\sum_{i,j} p_{ij} \cdot \phi(d_{ij}, \hat{d}_{ij})^2}{\sum_{i,j} p_{ij} + \epsilon}} \quad (7)$$

Similarly, the type loss \mathcal{L}_t is calculated as the masked BCE between \mathbf{T} and $\hat{\mathbf{T}}$:

$$\mathcal{L}_t = \frac{\sum_{i,j} p_{ij} \cdot \text{BCE}(t_{ij}, \hat{t}_{ij})}{\sum_{i,j} p_{ij} + \epsilon} \quad (8)$$

IV. EXPERIMENTAL RESULTS

This section evaluates LEADER, demonstrating that a lightweight end-to-end network can achieve top-tier performance across diverse fingerprint modalities using a single, fixed set of weights. We assess the model's accuracy, efficiency, and generalization through the following experimental structure: Sec. IV-A describes the datasets and evaluation protocol, followed by a comparative analysis against established methods on both plain and latent fingerprints (Sec. IV-B). An ablation study then isolates the contributions of key structural components alongside the proposed CMR weighting strategy (Sec. IV-C). Finally, Sec. IV-D provides an interpretability analysis to investigate the internal representations learned by the model.

To ensure full reproducibility, comprehensive details regarding data augmentation, optimizer schedules, and hyperparameters—including an analysis of the training dynamics—are provided in Appendix C of the Supplementary Material.

A. Experimental Setup

LEADER is trained and evaluated using a heterogeneous collection of fingerprint datasets (Table II, Fig. 5), encompassing a wide spectrum of sensor technologies and noise patterns characteristic of real-world applications.

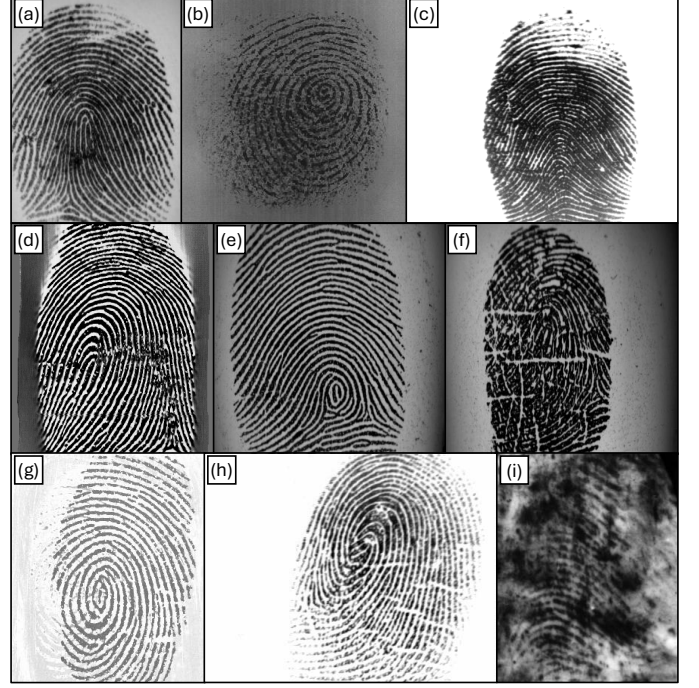


Fig. 5. Representative fingerprint samples from the datasets. The collection covers diverse acquisition technologies: (a) FVC2002 DB2-A (Optical); (b) FVC2002 DB3-A (Capacitive); (c) FVC2004 DB1-A (Optical); (d) FVC2004 DB3-A (Thermal sweeping); (e) FFE Good (Optical); (f) FFE Bad (Optical); (g) FVC2000 DB2-A (Capacitive); (h) FVC2002 DB1-A (Optical); (i) NIST SD27 (Latent).

1) *Training and Tuning Datasets*: The training set comprises 2,560 plain fingerprints derived from six distinct sources, containing a total of 92,084 ground-truth minutiae. We include subsets from the FVC2002 [24] and FVC2004 [25] benchmarks to expose the network to diverse ridge patterns and sensor-specific artifacts. Specifically, FVC2002 DB2-A and DB3-A introduce variations in skin moisture and exaggerated finger rotation, while the FVC2004 subsets (DB1-A, DB3-A) present severe skin distortions, varying contact pressure, and noise from excessively wet or dry fingers. FVC2004 DB3-A (thermal sweeping sensor) is particularly challenging due to reconstruction artifacts. To enhance the

TABLE II
CHARACTERISTICS OF THE DATASETS USED FOR TRAINING, HYPERPARAMETER TUNING, AND TESTING.

Dataset	Sensor Type	Fingers	Impressions	Total	Ground-truth Source ¹	Minutiae	Usage
FVC2002 DB2-A	Optical	100	1 ²	100	Manual (Authors)	5 041	
FVC2002 DB3-A	Capacitive	100	8	800	[19] [20]	19 032	
FVC2004 DB1-A	Optical	100	8	800	[19] [20]	32 771	
FVC2004 DB3-A	Thermal Sweeping	100	8	800	[19] [20]	32 608	Training
FFE Good	Optical	10	1	10	[21] ³	525	
FFE Bad	Optical	50	1	50	[21] ³	2 107	
FVC2000 DB2-A	Capacitive	100	1 ⁴	100	Manual (Authors)	4 298	Tuning
FVC2002 DB1-A	Optical	100	1 ⁴	100	[19] [20]	4 071	
NIST SD27	Latent	258	1	258	[22] [23]	5 303	Testing

¹ When two references are cited, the first refers to the segmentation mask and the second to the minutiae ground-truth.

² Only the third impression of each finger was used.

³ FFE ground-truth minutiae were extracted from manually-labeled ridge skeletons using the traditional crossing number method.

⁴ Only the first impression of each finger was used.

model’s capacity to handle fine structural details in both high- and low-quality fingerprints, the FFE Good and FFE Bad datasets from [21] are incorporated: the former contains high-quality samples, while the latter focuses on fingerprints affected by cuts, abrasions, and severe skin-moisture variations. Ground-truth segmentation masks for training samples are employed exclusively during data augmentation, as detailed in Appendix C (Supplementary Material).

Hyperparameters, including those governing the CMR encoding strategy (see Sec. III-C), are tuned using the first impression of each finger in FVC2000 DB2-A [26]. This dataset consists of fingerprints acquired from untrained users without quality control, providing a representative baseline for parameter optimization.

2) *Test Datasets*: The performance is evaluated on two held-out test sets to assess generalization capabilities. The first, FVC2002 DB1-A [24], represents a standard evaluation benchmark for plain optical fingerprints. The second, NIST SD27 [23], features latent fingerprints recovered from crime scenes. These samples present the most significant challenges, characterized by heavy background clutter, partial ridge structures, and environmental noise. Minutiae for this set were validated by professional latent examiners [23], while segmentation masks were sourced from [22].

3) *Evaluation Metrics and Protocol*: Performance in minutiae extraction is typically assessed through either *intrinsic evaluation*, which compares extracted minutiae directly against ground truth, or *extrinsic evaluation* based on recognition accuracy (e.g., EER). This work adopts the former to decouple performance from the biases of minutiae-comparison algorithms, which may mask extractor inaccuracies (such as errors in position, direction, or type) by means of error-tolerant heuristics. The evaluation follows a systematic protocol based on four steps:

- (i) *Minutiae pairing and filtering*—Extracted and ground-truth minutiae are paired by solving the assignment problem [27]. A match is defined as a True Positive (TP) if the Euclidean distance $\rho(\cdot)$ and angular difference $\phi(\cdot)$ are within thresholds ρ_t and θ_t , respectively. We adopt three increasingly stringent levels: $(\rho_t = 16 \text{ px}, \theta_t = \pi/6 \text{ rad})$, $(12, \pi/8)$, and $(8, \pi/10)$. To ensure objective comparison, all fingerprints are cropped to the ridge-area bounding box defined by ground-truth masks. Furthermore, minutiae within a 14 px margin of the segmentation boundary are excluded. While LEADER is inherently robust to boundary-induced spurious detections, this filtering is applied uniformly to avoid penalizing competitors for easily mitigable artifacts.
- (ii) *Aggregate performance computation*—Based on the pairing results, we report Precision-Recall (PR) curves and the F_1 -score at the optimal operating point. For methods providing quality scores (including LEADER), full PR curves are generated; for others, individual operating points are plotted. Both *type-agnostic* and *type-aware* regimes are considered, where the latter requires matching minutia types for a TP.
- (iii) *Sample-level ranking*—To assess consistency, extractors are ranked by the F_1 -score achieved on each fingerprint,

computed at the previously identified optimal operating point. We report the mean rank (with standard deviation) and the frequency of achieving top or top-3 positions. Furthermore, the *bottom half percentage* tracks how often a method falls into the lower 50% of the competitor pool, serving as a proxy for reliability. Finally, a pairwise *direct-win* analysis quantifies how often a method outperforms each specific competitor on a per-sample basis.

- (iv) *Efficiency analysis*—Computational cost is evaluated in terms of execution latency (on both CPU and GPU) to assess suitability for real-time applications.

B. Performance Evaluation and Comparative Analysis

To ensure a rigorous and transparent evaluation, LEADER is compared against a broad spectrum of established methods by executing official implementations on the specified test datasets. This approach is adopted to eliminate *cross-protocol bias* that often affects academic comparisons, where performance discrepancies may arise from disparate minutiae-pairing heuristics, varying spatial or angular thresholds, or inconsistent handling of image boundaries. By processing all methods through the same evaluation pipeline described in Sec. IV-A, performance variations are attributable solely to the extraction algorithms. The selected methods represent three distinct categories:

- *SOTA Deep Learning Models*: FingerNet [11], MinutiaeNet [12], and LatentAFIS [15]. These are the open-source neural architectures identified in Table I.
- *COTS Solutions*: FingerJet OSE [28], FDx v4.31 [29], and VeriFinger v13.1 [30]. These engines facilitate an assessment of the industrial relevance of LEADER against production-grade software.
- *Standard Baselines and Independent Projects*: MINDTCT [31], FingerFlow [32], and SourceAFIS [33]. This group includes traditional baselines and open-source contributions. While these projects lack formal peer-reviewed publications, they represent widely accessible tools within the fingerprint community.

The comparative evaluation results, summarized in Table III and Figure 6, indicate that LEADER consistently outperforms all competitors across all datasets and evaluation regimes. On the FVC2002 DB1-A benchmark, LEADER achieves a peak F_1 -score of 0.92, surpassing specialized deep-learning models such as FingerNet (0.87) and LatentAFIS (0.84), as well as high-tier commercial engines (VeriFinger and FDx, both 0.86). Notably, LEADER demonstrates high stability under stringent threshold levels: the F_1 -score remains as high as 0.90 at $(8 \text{ px}, \pi/10 \text{ rad})$, whereas competitors experience sharper declines. This precision is further substantiated by the PR curves in Figure 6. The superiority of the proposed architecture is even more pronounced in the *type-aware* regime, where LEADER maintains a 0.12 absolute margin over the leading commercial competitor (FDx). This suggests that the two autoencoders effectively extract the high-level features necessary for accurate classification of ridge endings and bifurcations. In the cross-domain evaluation on NIST SD27, LEADER exhibits robust zero-shot generalization, achieving the highest F_1 -score

TABLE III

COMPARATIVE PERFORMANCE (F_1 -SCORE). RESULTS ARE REPORTED FOR THE THREE THRESHOLD LEVELS UNDER BOTH TYPE-AGNOSTIC AND TYPE-AWARE EVALUATION REGIMES. **BOLD** AND UNDERLINED VALUES INDICATE THE BEST AND SECOND-BEST SCORES, RESPECTIVELY.

Method	FVC2002 DB1-A			NIST SD27		
	(16 px, $\pi/6$ rad)	(12 px, $\pi/8$ rad)	(8 px, $\pi/10$ rad)	(16 px, $\pi/6$ rad)	(12 px, $\pi/8$ rad)	(8 px, $\pi/10$ rad)
Type-agnostic	FingerNet	0.87	0.86	0.83	0.67	0.64
	LatentAFIS	0.84	0.83	0.81	0.62	0.59
	MinutiaeNet	0.47	0.43	0.38	0.48	0.45
	FingerJet	0.83	0.80	0.75	0.40	0.36
	FDx	0.86	0.85	0.81	0.45	0.41
	VeriFinger	0.86	0.85	0.80	0.64	0.61
	MINDTCT	0.84	0.82	0.78	0.32	0.29
	FingerFlow	0.53	0.49	0.43	0.49	0.47
	SourceAFIS	0.78	0.76	0.72	0.29	0.25
Type-aware	LEADER (Ours)	0.92	0.91	0.90	0.71	0.69
	FingerJet	0.64	0.62	0.58	0.27	0.25
	FDx	<u>0.73</u>	<u>0.71</u>	<u>0.69</u>	0.30	0.28
	VeriFinger	0.71	0.70	0.67	<u>0.42</u>	<u>0.39</u>
	MINDTCT	0.72	0.70	0.66	0.21	0.19
	FingerFlow	0.34	0.31	0.27	0.29	0.27
	SourceAFIS	0.62	0.60	0.58	0.19	0.17
	LEADER (Ours)	0.85	0.84	0.83	0.52	0.51
						0.47

(0.71) on latent fingerprints despite being trained exclusively on plain impressions. It outperforms both commercial systems (VeriFinger, 0.64) and specialized models such as FingerNet (0.67) and LatentAFIS (0.62), which were exposed to the latent domain during training. As shown in Figure 6, the proposed model maintains higher precision across the entire recall range. This margin increases in the *type-aware* regime: at the most stringent thresholds, LEADER outperforms the second-best method (VeriFinger) by 34% (0.47 vs 0.35 F_1 -score). These results suggest that LEADER learns domain-transferable topological features that generalize more effectively than those of larger or domain-specific models—a characteristic further analyzed in Section IV-D.

To evaluate reliability of performance across each dataset, the comparative analysis is extended to a sample-level ranking computed at the (16 px, $\pi/6$ rad) thresholds. As detailed in Table VII (Appendix D of the Supplementary Material), LEADER obtains an average rank of 1.43 ± 0.83 on FVC2002 DB1-A and 2.07 ± 1.30 on NIST SD27. The proposed method consistently dominates its competitors, as further evidenced by the pairwise direct-win matrices in Tables VIII–IX. On FVC2002, LEADER surpasses the second-best method (FingerNet) in 85% of the samples, while being outperformed by it in only 13% of cases. This margin is further highlighted by the frequency of achieving the top-ranking position: LEADER secures first place in 71% of cases, exceeding the 13% achieved by FingerNet by a factor of five. Even on the challenging NIST SD27, LEADER outperforms FingerNet in 64% of the samples (compared to 29% for the runner-up) and remains the top-ranked extractor for 47% of the instances. Overall, the proposed method achieves a top-three position in 96% of plain fingerprints and 84% of latent ones, falling into the bottom half of the ranking in only 1% of the NIST SD27 samples. The consistency of these statistical trends is qualitatively supported by the sample-level visual analysis in Fig. 7. In high-performance instances (rows 1 and 3), LEADER

demonstrates superior localization and marked reduction in spurious detections compared to established methods. Even in its lowest-performing plain-fingerprint case (Fig. 7d), the model remains competitive with an F_1 -score of 0.75; notably, several false positives in this sample correspond to valid minutiae omitted from the ground truth. Finally, the failure case in Fig. 7j underscores that minutiae extraction in heavily corrupted impressions remains an open challenge.

Regarding computational efficiency, Table IV reports average processing times. With a compact footprint of 0.9 M parameters, the proposed architecture achieves an average GPU inference time of 15 ms. LEADER maintains a competitive runtime of 322 ms on CPU, outperforming commercial engines such as FDx and VeriFinger. While the CPU execution of competing deep-learning architectures [11], [12], [15] scales poorly, the proposed model remains viable for real-time applications on general-purpose processors. Modern community-driven implementations such as FingerFlow, which extend [12] with additional neural stages, exhibit significantly higher latency (7068 ms on GPU), justifying the lightweight and integrated design of LEADER. These results indicate that the model provides a favorable trade-off between structural complexity and throughput, suitable for both server-side processing and edge-device deployment.

C. Ablation Study

To evaluate the contribution of individual architectural components, Table V summarizes a systematic ablation study. The empirical evidence reveals a performance dichotomy between the two datasets. For plain fingerprints (FVC2002 DB1-A), removing individual components (rows 1–5) leads to negligible degradation, with *type-agnostic* F_1 -scores remaining above 0.87. Conversely, on latent fingerprints (NIST SD27), identical simplifications induce pronounced performance drops. For instance, removing the *Attention-Gate* or the *Refinement-Autoencoder* reduces the *type-agnostic* F_1 -score from 0.71 to

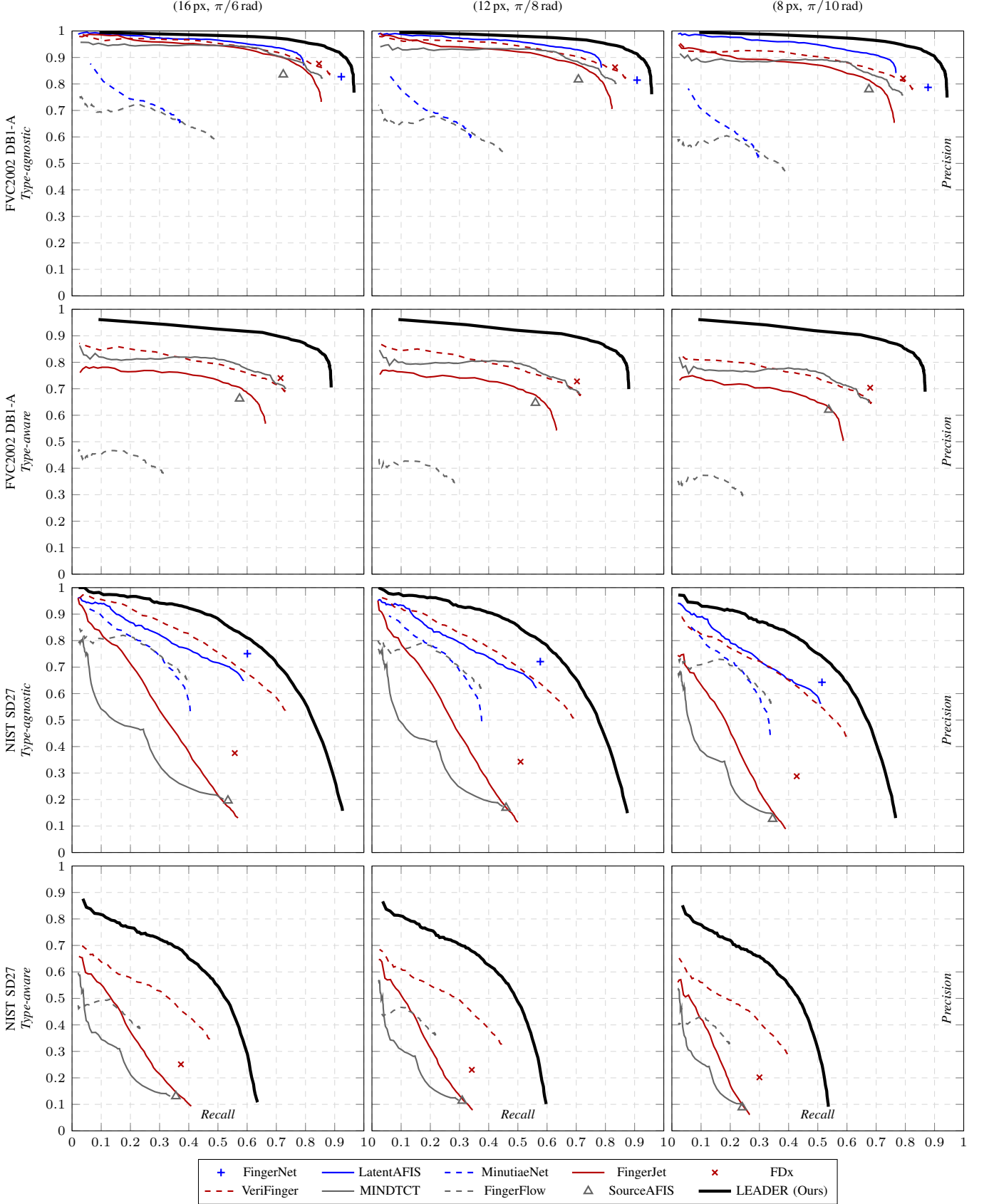


Fig. 6. PR curves for FVC2002 DB1-A (top two rows) and NIST SD27 (bottom two rows). Each column represents a different threshold level, from the most permissive (16 px, $\pi/6$ rad) to the most demanding (8 px, $\pi/10$ rad). Results are reported for both *type-agnostic* and *type-aware* regimes. For methods that do not support minutiae type (FingerNet, LatentAFIS, and MinutiaeNet), curves are omitted from *type-aware* plots to ensure a fair comparison while maintaining legend consistency.

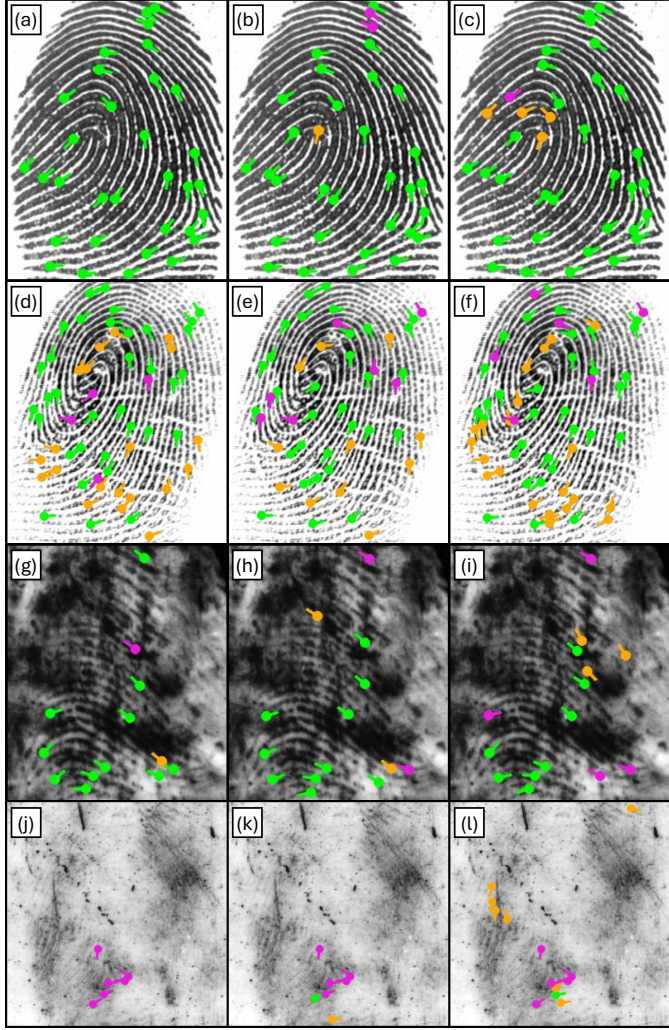


Fig. 7. **Sample-level visual comparisons.** True Positives (green), False Positives (orange), and False Negatives (magenta) are overlaid for LEADER and the two top-performing competitors. Rows illustrate representative performance scenarios: (a–c) high-scoring sample on FVC2002 DB1-A; (d–f) LEADER’s lowest-performing case on FVC2002 DB1-A; (g–i) high-scoring latent sample on NIST SD27; (j–l) failure case on NIST SD27. First column (a, d, g, j) shows LEADER results (F_1 -score: 1.0, 0.75, 0.92, 0.00). Second and third columns display top competitors: (b) FDx (0.95), (c) MINDTCT (0.93), (e) LatentAFIS (0.77), (f) FingerJet (0.71), (h) VeriFinger (0.83), (i) FingerJet (0.70), (k) LatentAFIS (0.25), and (l) FDx (0.14). Full-image comparisons for all extractors are provided in Figs. 18–21 (Supplementary Material).

0.64 and 0.59, respectively. These results confirm that while a shallower model may suffice for high-quality samples, the full hierarchical depth and attention mechanism of LEADER are essential for resolving ambiguous ridge structures in low-quality impressions. A key finding is the non-linear performance collapse observed in combined ablation scenarios (rows 6–9). The data reveal a synergistic interaction between the initial feature extraction and the CMR encoding strategy. Specifically, while the independent removal of the *Stem* (row 1) or the adoption of standard Gaussian encoding (row 5) reduces the latent F_1 -score by 0.05 and 0.15, respectively, their simultaneous application (row 6) triggers a disproportionate collapse of 0.33 (from 0.71 to 0.38). This degradation significantly exceeds the additive drop (0.20), indicating

TABLE IV
AVERAGE EXECUTION TIME (MS) ON NIST SD27.

Method	Parameters (M)	Time (ms)
CPU ¹	FingerNet	4.7
	LatentAFIS	5.5
	MinutiaeNet	74.4
	FingerJet	—
	FDx	—
	VeriFinger	—
	MINDTCT	—
	FingerFlow	291.3
	SourceAFIS	—
GPU	LEADER (Ours)	0.9
	FingerNet	4.7
	LatentAFIS	5.5
	MinutiaeNet	74.4
	FingerFlow	291.3
	LEADER (Ours)	0.9
		15^{3,4}

¹ Intel® Xeon® CPU @ 2.60 GHz.

² GPU runtimes reported from original papers [11], [12], [15] due to legacy framework dependencies incompatible with modern software stacks.

³ NVIDIA RTX™ 3080 Ti GPU.

⁴ Average inference time measured with batch size 32.

a non-linear coupling between the *Stem* and CMR. Their joint absence triggers a systemic failure that the remaining architecture cannot mitigate, proving they are collectively essential for robust performance in latent scenarios. Finally, the configuration comprising only the *Head* (row 9) fails to generalize ($F_1 = 0.0$), despite reaching training convergence. This highlights that minutiae extraction cannot be reduced to a simple mapping but requires the global topological supervision provided by the CMR strategy and the multi-stage refinement pipeline.

D. Visual Analysis and Feature Interpretability

Fig. 8 visualizes the output maps generated for a high-quality fingerprint region. The position map $\hat{\mathbf{P}}$ (Fig. 8b) and its refined version $\tilde{\mathbf{P}}$ (Fig. 8c) demonstrate how the network translates ridge topology into localized confidence peaks. Notably, only genuine minutiae survive the threshold $\tau_q = 0.6$, an operating point consistent with the experimental evaluation. The direction and type maps, $\hat{\mathbf{D}}$ and $\hat{\mathbf{T}}$ (Figs. 8d–

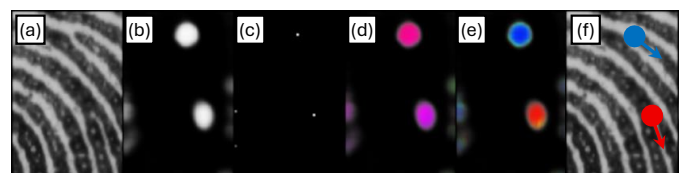


Fig. 8. **Visualization of output maps and decoding logic.** (a) Input fingerprint region. (b) Predicted position map $\hat{\mathbf{P}}$. (c) Refined map $\tilde{\mathbf{P}}$ showing local peaks. (d) Direction map $\hat{\mathbf{D}}$: the angle \hat{d}_{ij} is mapped to the Hue component (HSV); the two blobs show distinct shades of magenta, corresponding to the directions of the two minutiae, approximately $-\pi/5$ (top) and $-\pi/3$ (bottom). (e) Type map $\hat{\mathbf{T}}$: Hue encodes the classification score \hat{t}_{ij} on a gradient from red (bifurcation) to blue (ridge ending). In (d) and (e), *Saturation* and *Value* are modulated by \hat{p}_{ij} to suppress background noise. (f) Final extracted set $\hat{\mathbb{M}}$.

TABLE V

ABLATION STUDY. PERFORMANCE (F_1 -SCORE) EVALUATED ACROSS THE THREE THRESHOLD LEVELS FOR BOTH TYPE-AGNOSTIC AND TYPE-AWARE REGIMES, COMPARING THE FULL LEADER ARCHITECTURE AGAINST VARIOUS DEGRADED CONFIGURATIONS.

#	Configuration ¹						Type-agnostic						Type-aware					
	S	CA	AG	RA	GTE	FVC2002 DB1-A			NIST SD27			FVC2002 DB1-A			NIST SD27			
						(16, $\frac{\pi}{6}$)	(12, $\frac{\pi}{8}$)	(8, $\frac{\pi}{10}$)	(16, $\frac{\pi}{6}$)	(12, $\frac{\pi}{8}$)	(8, $\frac{\pi}{10}$)	(16, $\frac{\pi}{6}$)	(12, $\frac{\pi}{8}$)	(8, $\frac{\pi}{10}$)	(16, $\frac{\pi}{6}$)	(12, $\frac{\pi}{8}$)	(8, $\frac{\pi}{10}$)	
0	✓	✓	✓	✓	✓	■	0.92	0.91	0.90	0.71	0.69	0.62	0.85	0.84	0.83	0.52	0.51	0.47
1	—	✓	✓	✓	✓	■	0.91	0.90	0.88	0.66	0.63	0.56	0.82	0.81	0.80	0.47	0.45	0.41
2	✓	—	✓	✓	✓	■	0.91	0.91	0.90	0.64	0.61	0.54	0.83	0.83	0.82	0.46	0.44	0.41
3	✓	✓	—	✓	✓	■	0.91	0.91	0.90	0.64	0.61	0.55	0.84	0.83	0.82	0.46	0.45	0.41
4	✓	✓	✓	✓	—	■	0.90	0.89	0.87	0.59	0.56	0.49	0.81	0.80	0.79	0.43	0.41	0.37
5	✓	✓	✓	✓	✓	●	0.90	0.90	0.88	0.56	0.53	0.47	0.83	0.82	0.81	0.43	0.41	0.37
6	—	✓	✓	✓	✓	●	0.85	0.82	0.76	0.38	0.33	0.27	0.74	0.71	0.67	0.28	0.25	0.21
7	—	—	✓	✓	●	●	0.71	0.65	0.58	0.28	0.22	0.16	0.60	0.56	0.51	0.20	0.16	0.12
8	—	—	—	✓	●	●	0.70	0.64	0.56	0.26	0.21	0.15	0.59	0.55	0.49	0.19	0.15	0.12
9	—	—	—	—	●	●	0.00	0.00	0.00	0.00	0.00	0.00	0.00	0.00	0.00	0.00	0.00	0.00

¹ **S:** Stem; **CA:** Context-Autoencoder; **AG:** Attention-Gate; **RA:** Refinement-Autoencoder; **GTE:** Ground-Truth Encoding (■ CMR, ● Gaussian).

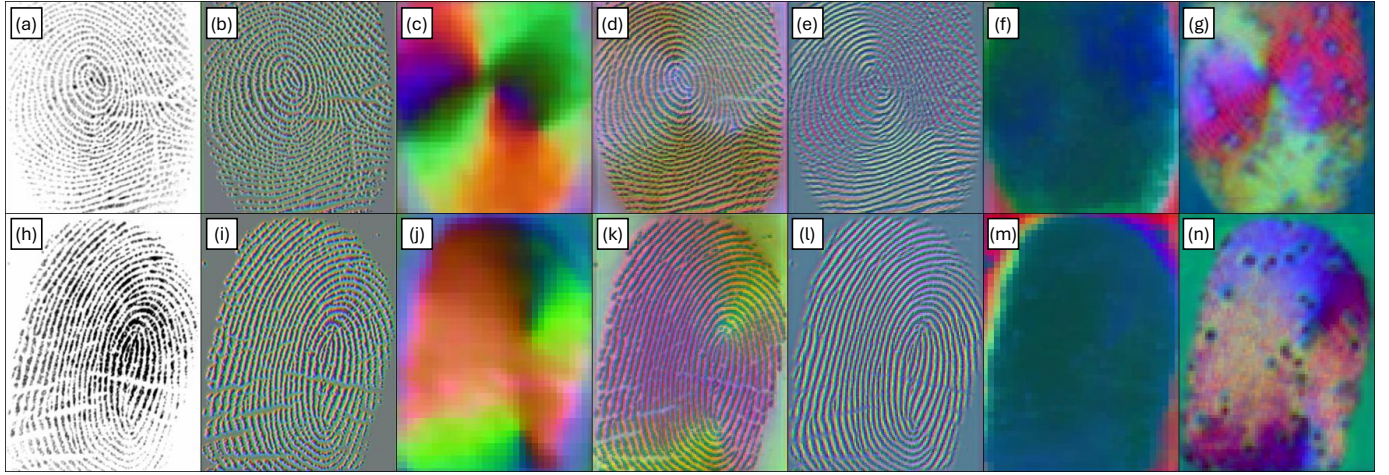


Fig. 9. **Visual analysis of internal features through PCA projection.** (a, h) Input fingerprints from FVC2002 DB1-A. (b–g, i–n) RGB visualization of the first three principal components of the feature maps. All visualized activations are generated via GELU, except for (d, k), which correspond to the Sigmoid gating signal \mathbf{X}_{gate} from the *Attention-Gate*. (b, i) First *StemBlock*. (c, j) Second *SeparableConvBlock* in the encoding path of the *Context-Autoencoder*. The remaining panels illustrate successive *InvBottleneckConvBlock* activations within the *Refinement-Autoencoder*: (e, l) first in encoding, (f, m) penultimate in decoding, and (g, n) final in decoding.

e), confirm the precision of the *Head* in regressing directions and discriminating types, resulting in a highly accurate set $\hat{\mathbb{M}}$.

While the output maps in Fig. 8 demonstrate decoding accuracy, they do not reveal how the architecture captures the fundamental principles of fingerprint topology. To uncover internal representations, Principal Component Analysis (PCA) is applied to the activations of key layers. For each selected layer, feature vectors are collected from all pixels across the first half of the FVC2002 DB1-A dataset. These high-dimensional vectors are projected onto a three-dimensional subspace defined by the first three principal components and normalized within the global range. Mapping these components to the RGB color space enables direct visualization of the internal representation, as illustrated in Fig. 9. Early representations produced by the *Stem* (Fig. 9b, i) emphasize local gradients, serving as a multi-scale edge detection stage. A more complex behavior emerges in the *Context-Autoencoder* (Fig. 9c, j), where the color distribution correlates with local ridge orientation. Notably, the network has autonomously discovered the importance of the orientation field—a corner-

stone of traditional fingerprint analysis [34]—and learned to encode it without explicit supervision (as validated by the ideal angular response in Fig. 11b). The *Attention-Gate* signal \mathbf{X}_{gate} (Fig. 9d, k) reveals a dual role: it tracks both orientation and localized noise, such as the prominent ridge cuts in the second sample, which are selectively dampened to stabilize subsequent extraction (see Fig. 10). In the early encoding stages of the *Refinement-Autoencoder* (Fig. 9e, l), the model performs a *neural thinning* process. The network generates an enhanced skeleton-like representation of ridges and valleys, effectively using a learned inpainting mechanism to close gaps caused by cuts. This suggests the emergence of a topological prior that maintains ridge continuity (see Fig. 10f). In the final stages of the *Refinement-Autoencoder* (Fig. 9f, m), the dominant feature becomes foreground-background segmentation. While traditional methods typically perform segmentation as a preprocessing step [35], LEADER treats it as a high-level semantic attribute learned during final refinement. This layer also appears to encode local ridge frequency [21], whose emergence is isolated in the frequency-gradient analysis of

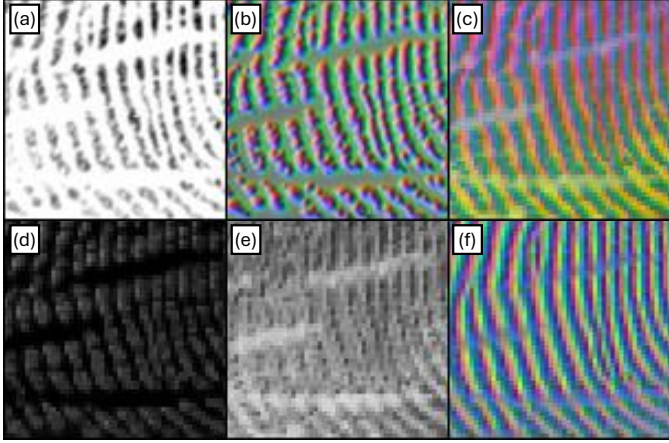


Fig. 10. **Analysis of ridge cut robustness.** The sequence focuses on the bottom-left region of the fingerprint in Fig. 9h: (a) raw input; (b) PCA projection of *Stem* features; (c) PCA projection of the *Attention-Gate* signal \mathbf{X}_{gate} ; (d, e) individual \mathbf{X}_{gate} channels exhibiting noise reduction and localized noise focusing; (f) topological inpainting and neural thinning in the PCA projection of *Refinement-Autoencoder* features.

Fig. 11g. Finally, the pre-head feature maps (Fig. 9g, n) consolidate all relevant information, effectively encoding both orientation and minutiae candidates to provide the necessary context for task-specific processing.

To investigate LEADER’s robustness, Fig. 10 provides a detailed view of the response to deep ridge cuts. While early *Stem* activations (Fig. 10b) treat these scratches as valid structural gradients, the *Attention-Gate* performs a multi-channel decomposition of the noise. Individual channels of \mathbf{X}_{gate} exhibit specialized behaviors: some serve as suppression masks by mapping noise to near-zero values (Fig. 10d), while others highlight noise patterns (Fig. 10e), likely providing a spatial *invalidity map* to guide subsequent reconstruction. The resulting neural thinning (Fig. 10f) does not merely ignore noise but performs topological inpainting. Ridges are reconnected across the cuts with high chromatic continuity; the slightly fainter hue observed at scratch locations suggests that the network projects the ridge flow based on global context while retaining a trace of the missing original information. This emergent ability to restore ridge topology represents a significant advantage over traditional processing pipelines.

To isolate the response to fundamental geometric properties, LEADER is evaluated on two synthetic patterns: concentric circles with constant frequency (Fig. 11a) and horizontal ridges with varying frequency (Fig. 11e). PCA projections confirm the decoupling of these emergent features. In the *Context-Autoencoder*, the model behaves as a specialized orientation extractor: it produces a continuous chromatic shift for the circles (Fig. 11b) while maintaining a nearly uniform hue for the horizontal ridges (Fig. 11f), as expected for a constant orientation field. Conversely, the *Refinement-Autoencoder* captures frequency variations: it exhibits a vertical gradient for the varying-frequency pattern (Fig. 11g), whereas it yields a homogeneous response for the constant-frequency circles (Fig. 11c). The final representation (Fig. 11d, h) synthesizes both attributes, demonstrating that LEADER has developed

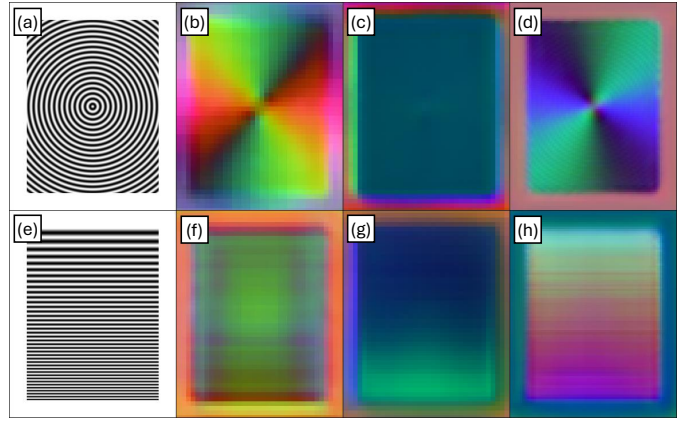


Fig. 11. **Internal representation of synthetic geometric patterns.** Features are visualized via PCA projection. Top row (a–d): Concentric circles (constant frequency). Bottom row (e–h): Horizontal ridges (varying frequency). Columns: (a, e) input; (b, f) orientation-sensitive features (*Context-Autoencoder*); (c, g) frequency/segmentation features (*Refinement-Autoencoder*); (d, h) final common representation.

universal signal-processing primitives for quasi-periodic patterns.

V. CONCLUSION

In this work, we introduced LEADER, a lightweight end-to-end architecture for minutiae extraction that maps raw fingerprint images directly to comprehensive minutiae attributes through an integrated on-graph pipeline. By consolidating the extraction and refinement stages within a single neural manifold, LEADER eliminates the requirement for external postprocessing or handcrafted heuristics, while achieving SOTA performance with only 0.9 M parameters. Across two heterogeneous benchmarks, the proposed model demonstrates superior precision and reliability, maintaining high F_1 -scores even under stringent threshold levels, where existing methods exhibit significant performance degradation. Sample-level ranking analysis confirms this systematic superiority, with the model consistently outperforming both deep learning-based competitors and established commercial engines on individual samples.

A key finding of our study is the model’s robust cross-domain generalization. Despite being trained exclusively on plain fingerprints, LEADER’s ability to learn fundamental topological structures allows it to outperform specialized systems on the NIST SD27 latent dataset. The interpretability analysis revealed that the network autonomously discovers and decouples core biometric primitives, such as segmentation masks, orientation fields, ridge frequencies, and skeletons. The emergence of these representations, combined with the observed ability to perform topological inpainting over deep ridge cuts, suggests that LEADER has moved beyond simple pattern matching toward a deep, structural understanding of fingerprint morphology. This confirms that a relatively compact model, when guided by the proposed CMR topological supervision strategy, can achieve a level of abstraction that generalizes far better than larger, unconstrained architectures.

The computational efficiency inherent in this design further suggests a shift in the deployment paradigm of high-precision

biometrics. By delivering high-throughput inference with a minimal parameter count, LEADER demonstrates that sophisticated topological reasoning is possible without resource-intensive hardware, positioning our model as an ideal candidate for secure, local identification on mobile and IoT devices.

Despite these advances, the accurate recovery of features from severely degraded latent evidence remains an open frontier. Our analysis of low-performance cases underscores that extreme environmental noise and fragmented ridge structures can still exceed the reconstructive capabilities of current supervised models. Future research will explore self-supervised pre-training on large-scale unlabeled data, which may strengthen the model's ability to infer missing ridge structures and maintain topological consistency in highly corrupted samples.

REFERENCES

- [1] D. Maltoni, D. Maio, A. K. Jain, and J. Feng, *Handbook of Fingerprint Recognition*. Springer Nature Switzerland AG, 2022.
- [2] D. Maltoni, R. Cappelli, and D. Meuwly, *Automated Fingerprint Identification Systems: From Fingerprints to Fingermarks*. Cham: Springer International Publishing, 2017, pp. 37–61. [Online]. Available: https://doi.org/10.1007/978-3-319-50673-9_3
- [3] Z. Liu, H. Mao, C.-Y. Wu, C. Feichtenhofer, T. Darrell, and S. Xie, “A convnet for the 2020s,” in *2022 IEEE/CVF Conference on Computer Vision and Pattern Recognition (CVPR)*, 2022, pp. 11966–11976.
- [4] D. Maio and D. Maltoni, “Direct gray-scale minutiae detection in fingerprints,” *IEEE Transactions on Pattern Analysis and Machine Intelligence*, vol. 19, no. 1, pp. 27–40, 1997.
- [5] H. Fronthaler, K. Kollreider, and J. Bigun, “Local features for enhancement and minutiae extraction in fingerprints,” *IEEE Transactions on Image Processing*, vol. 17, no. 3, pp. 354–363, 2008.
- [6] K. G. Larkin and P. A. Fletcher, “A coherent framework for fingerprint analysis: are fingerprints holograms?” *Opt. Express*, vol. 15, no. 14, pp. 8667–8677, Jul 2007. [Online]. Available: <https://opg.optica.org/oe/abstract.cfm?URI=oe-15-14-8667>
- [7] A. Sankaran, P. Pandey, M. Vatsa, and R. Singh, “On latent fingerprint minutiae extraction using stacked denoising sparse autoencoders,” in *IEEE International Joint Conference on Biometrics*, 2014, pp. 1–7.
- [8] L. Jiang, T. Zhao, C. Bai, A. Yong, and M. Wu, “A direct fingerprint minutiae extraction approach based on convolutional neural networks,” in *2016 International Joint Conference on Neural Networks (IJCNN)*, 2016, pp. 571–578.
- [9] L. N. Darlow and B. Rosman, “Fingerprint minutiae extraction using deep learning,” in *2017 IEEE International Joint Conference on Biometrics (IJCB)*, 2017, pp. 22–30.
- [10] Y. Tang, F. Gao, and J. Feng, “Latent fingerprint minutiae extraction using fully convolutional network,” in *2017 IEEE International Joint Conference on Biometrics (IJCB)*, 2017, pp. 117–123.
- [11] Y. Tang, F. Gao, J. Feng, and Y. Liu, “Fingernet: An unified deep network for fingerprint minutiae extraction,” in *2017 IEEE International Joint Conference on Biometrics (IJCB)*. Denver, CO, USA: IEEE Press, 2017, p. 108–116. [Online]. Available: <https://doi.org/10.1109/BTAS.2017.8272688>
- [12] D.-L. Nguyen, K. Cao, and A. K. Jain, “Robust minutiae extractor: Integrating deep networks and fingerprint domain knowledge,” in *2018 International Conference on Biometrics (ICB)*, 2018, pp. 9–16.
- [13] V. H. Nguyen, J. Liu, T. H. B. Nguyen, and H. Kim, “Universal fingerprint minutiae extractor using convolutional neural networks,” *IET Biometrics*, vol. 9, no. 2, pp. 47–57, 2020.
- [14] B. Zhou, C. Han, Y. Liu, T. Guo, and J. Qin, “Fast minutiae extractor using neural network,” *Pattern Recognition*, vol. 103, p. 107273, 2020. [Online]. Available: <https://www.sciencedirect.com/science/article/pii/S0031320320300789>
- [15] K. Cao, D.-L. Nguyen, C. Tymoszek, and A. K. Jain, “End-to-end latent fingerprint search,” *IEEE Transactions on Information Forensics and Security*, vol. 15, pp. 880–894, 2020.
- [16] Z. Zhang, S. Liu, and M. Liu, “A multi-task fully deep convolutional neural network for contactless fingerprint minutiae extraction,” *Pattern Recognition*, vol. 120, p. 108189, 2021. [Online]. Available: <https://www.sciencedirect.com/science/article/pii/S0031320321003526>
- [17] Y. Feng and A. Kumar, “Detecting locally, patching globally: An end-to-end framework for high speed and accurate detection of fingerprint minutiae,” *IEEE Transactions on Information Forensics and Security*, vol. 18, pp. 1720–1733, 2023.
- [18] A. Malhotra, A. Sankaran, M. Vatsa, R. Singh, K. B. Morris, and A. Noore, “Understanding ace-v latent fingerprint examination process via eye-gaze analysis,” *IEEE Transactions on Biometrics, Behavior, and Identity Science*, vol. 3, no. 1, pp. 44–58, 2021.
- [19] D. H. Thai, S. Huckemann, and C. Gottschlich, “Filter design and performance evaluation for fingerprint image segmentation,” *PLOS ONE*, vol. 11, no. 5, pp. 1–31, 05 2016. [Online]. Available: <https://doi.org/10.1371/journal.pone.0154160>
- [20] M. Kayaoglu, B. Topcu, and U. Uludag, “Standard fingerprint databases: Manual minutiae labeling and matcher performance analyses,” 2013. [Online]. Available: <https://arxiv.org/abs/1305.1443>
- [21] R. Cappelli, “No feature left behind: Filling the gap in fingerprint frequency estimation,” *IEEE Access*, vol. 12, pp. 153605–153617, 2024. [Online]. Available: <https://doi.org/10.1109/ACCESS.2024.3481507>
- [22] J. Feng, J. Zhou, and A. K. Jain, “Orientation field estimation for latent fingerprint enhancement,” *IEEE Transactions on Pattern Analysis and Machine Intelligence*, vol. 35, no. 4, pp. 925–940, 2013.
- [23] M. D. Garris and R. M. McCabe, “NIST special database 27: Fingerprint minutiae from latent and matching tenprint images,” National Institute of Standards and Technology (NIST), Gaithersburg, MD, Tech. Rep. NISTIR 6534, Jun. 2000.
- [24] D. Maio, D. Maltoni, R. Cappelli, J. Wayman, and A. Jain, “Fvc2002: Second fingerprint verification competition,” in *2002 International Conference on Pattern Recognition*, vol. 3, 2002, pp. 811–814 vol.3.
- [25] R. Cappelli, D. Maio, D. Maltoni, J. Wayman, and A. Jain, “Performance evaluation of fingerprint verification systems,” *IEEE Transactions on Pattern Analysis and Machine Intelligence*, vol. 28, no. 1, pp. 3–18, 2006.
- [26] D. Maio, D. Maltoni, R. Cappelli, J. Wayman, and A. Jain, “Fvc2000: fingerprint verification competition,” *IEEE Transactions on Pattern Analysis and Machine Intelligence*, vol. 24, no. 3, pp. 402–412, 2002.
- [27] D. F. Crouse, “On implementing 2d rectangular assignment algorithms,” *IEEE Transactions on Aerospace and Electronic Systems*, vol. 52, no. 4, pp. 1679–1696, 2016.
- [28] DigitalPersona. Fingerprint feature extractor, open source edition. [Online]. Available: <https://github.com/FingerJetFXOSE/FingerJetFXOSE>
- [29] SecuGen. Fdx sdk. [Online]. Available: <https://secugen.com/products/sdk>
- [30] Neurotechnology. Verifinger sdk. [Online]. Available: <https://neurotechnology.com/verifinger.html>
- [31] C. I. Watson, M. D. Garris, E. Tabassi, C. L. Wilson, R. M. McCabe, S. Janet, and K. Ko, “User’s guide to nist biometric image software (nibus),” National Institute of Standards and Technology, techreport 7392, 2007.
- [32] J. Arendáč. Fingerflow. [Online]. Available: <https://github.com/jakubarendac/fingerflow>
- [33] R. Vazan. Sourceafis. [Online]. Available: <https://github.com/robertvazan/sourceafis-java>
- [34] R. Cappelli, “Exploring the power of simplicity: A new state-of-the-art in fingerprint orientation field estimation,” *IEEE Access*, vol. 12, pp. 55998–56018, 2024.
- [35] ———, “Unveiling the power of simplicity: Two remarkably effective methods for fingerprint segmentation,” *IEEE Access*, vol. 11, pp. 144530–144544, 2023.
- [36] J. L. Ba, J. R. Kiros, and G. E. Hinton, “Layer normalization,” 2016. [Online]. Available: <https://arxiv.org/abs/1607.06450>
- [37] D. Hendrycks and K. Gimpel, “Gaussian error linear units (gelus),” 2023. [Online]. Available: <https://arxiv.org/abs/1606.08415>
- [38] F. Chollet *et al.*, “Keras,” <https://keras.io>, 2015.
- [39] TensorFlow Developers, “Tensorflow: Large-scale machine learning on heterogeneous systems,” 2015, software available from tensorflow.org. [Online]. Available: <https://www.tensorflow.org/>
- [40] X. Chen, C. Liang, D. Huang, E. Real, K. Wang, H. Pham, X. Dong, T. Luong, C.-J. Hsieh, Y. Lu, and Q. V. Le, “Symbolic discovery of optimization algorithms,” in *Proceedings of the 37th International Conference on Neural Information Processing Systems*, ser. NIPS ’23. Red Hook, NY, USA: Curran Associates Inc., 2024.

LEADER: Lightweight End-to-End Attention-Gated Dual Autoencoder for Robust Minutiae Extraction

Raffaele Cappelli and Matteo Ferrara

APPENDIX A

MATHEMATICAL NOTATION

Table VI summarizes the mathematical notation used throughout this work, organized into three logical sections: (i) *Model and Inference*, covering input data, indexing, internal representations, and output data; (ii) *Ground-Truth-Encoding*, describing the topological supervision strategy; and (iii) *Training and Evaluation*, including the multi-task loss terms and the thresholds used for performance assessment.

Tensors and matrices are denoted by bold uppercase letters (e.g., \mathbf{P}, \mathbf{W}), while their individual elements at row i and column j are represented by the corresponding lowercase italics (e.g., p_{ij}, w_{ij}). Sets are denoted by blackboard bold letters (e.g., \mathbb{M}), and tuples or generic scalars by lowercase italics (e.g., m, r).

TABLE VI
MATHEMATICAL SYMBOLS AND NOTATION.

Symbol	Description
\mathbf{F}	Raw input fingerprint image
w, h	Width and height of the input image
i, j	Row and column indices of an element in the spatial grid
\mathbf{X}, \mathbf{X}'	Generic intermediate feature maps
\mathbf{X}_{gate}	Recalibration gating signal within the <i>Attention-Gate</i>
$\varsigma(\cdot)$	Sigmoid activation function
$[\cdot]$	Concatenation operator
\odot	Element-wise multiplication operator
Δ_r	Dilated convolution with rate r
$\hat{\mathbf{V}}_x, \hat{\mathbf{V}}_y$	Predicted Cartesian direction component maps
$\hat{\mathbf{P}}, \hat{\mathbf{D}}, \hat{\mathbf{T}}$	Predicted maps for position, direction, and type
$\tilde{\mathbf{P}}$	Predicted position map after on-graph NMS
$\hat{\mathbb{M}}, \hat{m}_k$	Extracted minutiae set and k -th minutia
\hat{x}_k, \hat{y}_k	Coordinates of \hat{m}_k
$\hat{\theta}_k, \hat{t}_k, \hat{q}_k$	Direction, type, and quality score of \hat{m}_k
τ_q	Confidence threshold for minutiae list extraction
<i>Model & Inference</i>	
\mathbb{M}, m_k	Ground-truth minutiae set and k -th minutia
x_k, y_k	Coordinates of m_k
θ_k, t_k	Direction and type of m_k
$\mathbf{P}, \mathbf{D}, \mathbf{T}$	Ground-truth maps for position, direction, and type
\mathbf{W}	Spatial weight map used for loss balancing
$\delta, \beta, \sigma, \lambda$	CMR encoding hyperparameters
$\omega(\cdot)$	CMR piece-wise weighting function
$\rho(\cdot)$	Euclidean distance
$\rho_{min}(\cdot)$	Euclidean distance to the nearest positive pixel in \mathbf{P}
$\mathcal{G}(\cdot)$	Gaussian function
<i>Ground-Truth Encoding</i>	
\mathcal{L}	Composite multi-task loss function
$\mathcal{L}_p, \mathcal{L}_d, \mathcal{L}_t$	Position, directional and type loss terms
$\alpha_p, \alpha_d, \alpha_t$	Hyperparameters for multi-task loss balancing
$\text{BCE}(\cdot)$	Binary Cross-Entropy function
$\phi(\cdot, \cdot)$	Wrapping angular difference function
ϵ	Small constant added for numerical stability
\mathcal{W}	Normalized weight magnitude (RMS of all parameters)
ρ_t, θ_t	Thresholds for ground-truth pairing
<i>Training & Evaluation</i>	

APPENDIX B

ARCHITECTURE AND COMPUTATIONAL LAYERS

This appendix provides a detailed hierarchical decomposition of the LEADER architecture, as illustrated in Figs. 12–16, along with the definitions of the primitive computational layers used throughout the network.

To ensure stable gradient flow and superior non-linear representation compared to traditional ReLU-based pipelines, LEADER consistently employs Layer Normalization [36] and GELU activation [37]. The following primitive operations form the building blocks of the architecture:

- *Conv*($c, s \times s$): Standard 2D convolution with c filters of size $s \times s$, and bias.
- *DConv*($c, s \times s, r$): Dilated 2D convolution with c filters of size $s \times s$, dilation rate r , and bias.
- *DepthwiseConv*($s \times s$): Parameter-efficient per-channel 2D convolution with kernel size $s \times s$, without bias.
- *Normalization*: Layer Normalization applied channel-wise.
- *Activation*(a): Computational layer applying function a , which can represent a non-linear activation (typically GELU or Sigmoid) or the identity mapping (Linear).
- *Pooling*($p, s \times s$): Spatial downsampling employing strategy p (Avg or Max), with an isotropic kernel size and stride of s .
- *Upsampling*($s \times s$): Spatial upsampling by a factor of s via nearest-neighbor interpolation.
- *SpatialDropout*: Regularization layer that randomly masks entire feature maps to prevent co-adaptation.
- *Concatenation / Split*: Channel-wise concatenation of feature maps or their separation into two equal halves.
- *Multiplication / Addition*: Element-wise operations used for feature gating and residual learning.
- *NonMaximumSuppression*: On-graph peak-finding layer (see Sec. III-B).
- *CartesianToPolar*: On-graph angular decoding layer (see Sec. III-B).

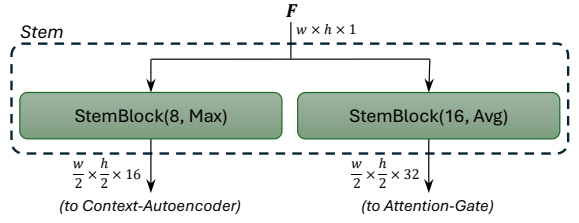


Fig. 12. **Stem component.** Detailed view of the dual-path input stage. It accepts the raw fingerprint \mathbf{F} and processes it through two specialized *StemBlocks* (detailed in Fig. 16d).

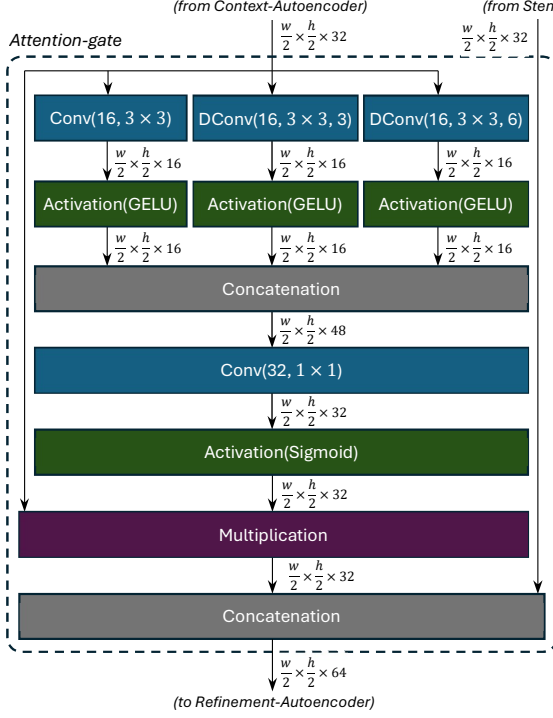


Fig. 13. **Attention-Gate component.** Internal flow of the recalibration mechanism. It computes the multi-scale gating signal \mathbf{X}_{gate} through parallel dilated paths and modulates the input features using element-wise multiplication before the final concatenation.

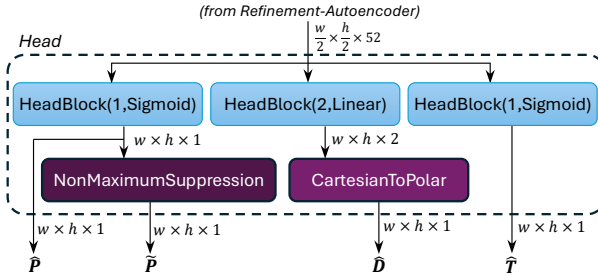


Fig. 14. **Head component.** Diagram of the task-specific decoding logic. The shared features are branched into three *HeadBlocks* (detailed in Fig. 16e) for position, direction, and type estimation. Task-specific activations are applied within each block: Sigmoid for position and type maps and Linear (identity) for the regression of Cartesian directional components. The pipeline concludes with on-graph NMS and *CartesianToPolar* angular decoding.

APPENDIX C IMPLEMENTATION AND TRAINING DETAILS

LEADER is implemented using the Keras framework [38] with the TensorFlow backend [39]. To promote a robust learning process across the heterogeneous datasets described in Sec. IV-A, we adopt the following protocol.

A. Data Preparation and Augmentation

To maintain a consistent input size, training samples are obtained by cropping patches of 256×320 pixels from the source images. Multiple patches per image are extracted to ensure full coverage of the ridge area while minimizing excessive overlap. To improve generalization, an extensive data

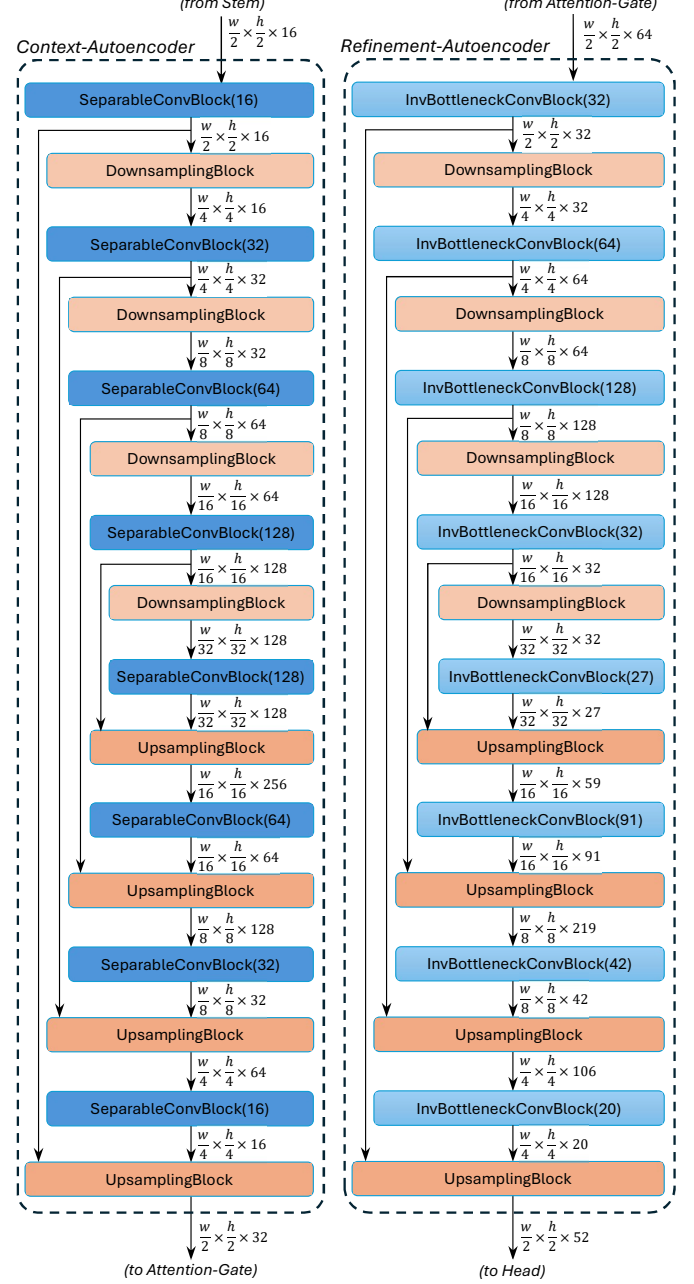


Fig. 15. **Context-Autoencoder and Refinement-Autoencoder components.** Side-by-side comparison: The *Context-Autoencoder* (left) employs *SeparableConvBlocks* for topological extraction (Fig. 16c), while the *Refinement-Autoencoder* (right) uses *InvBottleneckConvBlocks* for high-level semantic refinement (Fig. 16f). Both stages adopt *DownsamplingBlocks* and *UpsamplingBlocks* (Fig. 16a, b).

augmentation pipeline has been applied, including random translations, rotations ($\pm 90^\circ$), scaling ($\pm 25\%$), and flips, as well as gamma correction and contrast reduction. In addition, domain-specific perturbations simulate ridge thickness variations (through morphological erosion and dilation), alongside physical artifacts such as scratches and abrasions. During spatial transformations, empty regions are filled using constant padding based on the average background intensity—computed from ground-truth segmentation masks—to prevent high-contrast border artifacts.

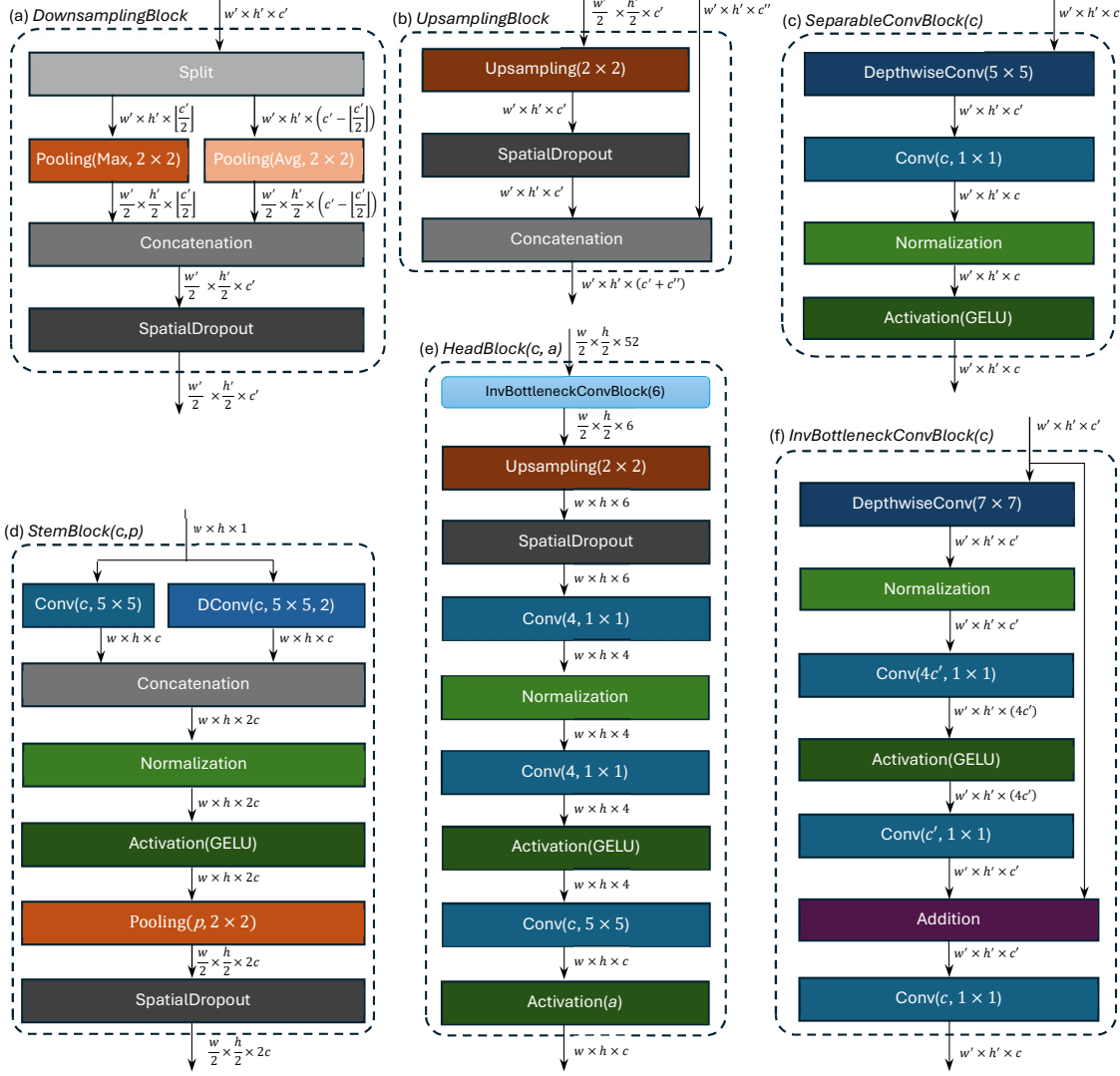


Fig. 16. **Computational block library.** Schematic of the modular blocks in LEADER: (a) *DownsamplingBlock* and (b) *UpsamplingBlock* for resolution management; (c) *SeparableConvBlock* for efficient feature extraction; (d) *StemBlock* for initial feature extraction and spatial mapping; (e) *HeadBlock* for task-specific projection; and (f) *InvBottleneckConvBlock*, the core building block of the *Refinement-Autoencoder*, designed for high-capacity representation with minimal parameter overhead. For blocks employed at multiple stages, input dimensions are denoted as $w' \times h' \times c'$ to indicate that the operation is resolution-agnostic and applicable to feature maps with varying spatial sizes and channel depths throughout the network.

B. Optimization and Training Strategy

LEADER is trained using the Lion optimizer [40] for a fixed duration of 25 epochs, each comprising 400 batches of size 32. The momentum parameters ($\beta_1 = 0.5, \beta_2 = 0.9$) are calibrated on the tuning set (Table II) to ensure stable convergence. The learning rate follows a cosine-decay schedule spanning the range $[10^{-6}, 3 \times 10^{-3}]$, which includes an initial warm-up phase. To mitigate overfitting, we integrate a weight decay of 0.35 and a spatial dropout rate of 2% (applied to the layers detailed in Appendix B). These regularization strategies, combined with the smooth convergence provided by the cosine-decay schedule, allow stable training without the need for a validation-based early stopping criterion.

Parameters for the CMR ground-truth encoding ($\delta = 4, \beta = 2, \sigma = 2, \lambda = 0.3$) and multi-task loss weights ($\alpha_p = 0.85, \alpha_d = 0.10, \alpha_t = 0.05$) are empirically selected using the tuning set (Table II). Training takes approximately 40 minutes

on an NVIDIA GeForce RTXTM 3080 Ti GPU.

The optimization dynamics are illustrated in Fig. 17, which reports the multi-task loss \mathcal{L} and the normalized weight magnitude \mathcal{W} (calculated as the RMS of all trainable parameters) across the training duration. The loss curve exhibits a rapid initial decrease followed by smooth asymptotic convergence, confirming both the efficacy of the selected hyperparameters and the stability of the Lion optimizer in this multi-task setting. Simultaneously, the trajectory of \mathcal{W} indicates a controlled evolution of the model capacity, where the weight magnitude stabilizes after the initial exploration phase.

APPENDIX D EXTENDED PERFORMANCE AND RANKING ANALYSIS

To further evaluate the robustness and consistency of LEADER against the competitors, this section provides an extended analysis comprising aggregate ranking statistics

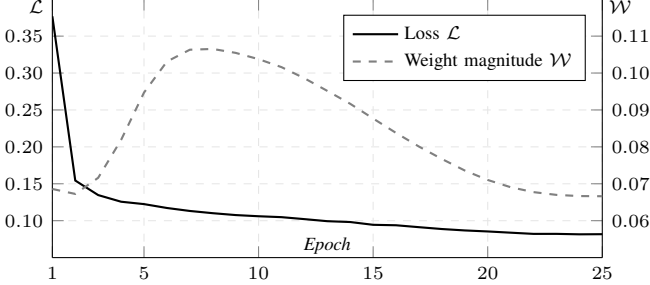


Fig. 17. **Optimization dynamics during LEADER training.** The primary axis (left) shows the minimization of the multi-task loss function \mathcal{L} . The secondary axis (right) illustrates the evolution of the normalized weight magnitude \mathcal{W} , indicating stable convergence and controlled model capacity.

and sample-level visual comparisons on FVC2002 DB1-A and NIST SD27. All evaluations in this section employ the (16 px, $\pi/6$ rad) threshold level under the *type-agnostic* regime.

Table VII reports comprehensive ranking statistics for the two datasets. This analysis demonstrates LEADER’s stability: it achieves the best average, top-1, and top-3 ranks and exhibits the lowest bottom half percentage on both datasets, underscoring its reliability even in challenging conditions.

To provide deeper insight, Tables VIII and IX present pairwise direct-win matrices, where each cell (i, j) denotes the percentage of samples in which method i outperforms method j in terms of F_1 -score. This fine-grained comparison highlights LEADER’s dominance, as it outperforms all other extractors in the vast majority of per-sample trials. These matrices also implicitly define the *tie rate* between any pair of extractors, which can be calculated as the remaining percentage after accounting for their reciprocal win rates.

Finally, figures 18–21 complement the aggregate statistics by providing four sample-level qualitative and quantitative assessments. These examples represent high- and low-performance cases (as determined by the F_1 -score) and offer a direct comparison of extraction accuracy under varying quality conditions.

TABLE VII
SAMPLE-LEVEL RANKING ANALYSIS. RESULTS SUMMARIZE MULTIPLE INDEPENDENT RANKINGS (ONE PER SAMPLE) BASED ON F_1 -SCORE COMPUTED AT THE (16 PX, $\pi/6$ RAD) THRESHOLD LEVEL IN THE TYPE-AGNOSTIC REGIME. **BOLD** AND UNDERLINED VALUES INDICATE THE BEST AND SECOND-BEST RESULTS FOR EACH METRIC, RESPECTIVELY.

Method	FVC2002 DB1-A				NIST SD27			
	Avg. Rank \pm S.D.	T1 (%)	T3 (%)	BH (%)	Avg. Rank \pm S.D.	T1 (%)	T3 (%)	BH (%)
FingerNet	3.48 ± 1.90	<u>13</u>	<u>56</u>	19	3.29 ± 2.16	<u>22</u>	<u>64</u>	15
LatentAFIS	4.98 ± 1.99	3	<u>27</u>	43	3.75 ± 1.84	11	<u>43</u>	<u>14</u>
MinutiaeNet	9.79 ± 0.41	0	0	100	5.36 ± 2.42	5	24	48
FingerJet	5.80 ± 1.73	1	10	62	7.36 ± 2.05	0	5	80
FDx	4.04 ± 1.85	8	43	22	6.18 ± 1.93	1	9	62
VeriFinger	3.74 ± 1.48	5	46	<u>12</u>	3.45 ± 1.85	15	<u>59</u>	16
MINDTCT	5.06 ± 1.89	4	25	47	8.41 ± 1.64	0	2	93
FingerFlow	9.16 ± 0.46	0	0	100	5.55 ± 2.46	8	23	56
SourceAFIS	7.13 ± 1.29	0	2	86	8.25 ± 1.44	0	1	97
LEADER (ours)	1.43 ± 0.83	<u>71</u>	<u>96</u>	0	2.07 ± 1.30	47	<u>84</u>	1

Avg. Rank \pm S.D.: Mean rank and standard deviation across all samples (lower is better).

T1, T3: Percentage of samples achieving a Top-1 or Top-3 rank, respectively.

BH (Bottom Half): Percentage of samples falling into the lower 50% of the ranking (lower is better).

TABLE VIII
PAIRWISE DIRECT-WIN RATES (%) ON FVC2002 DB1-A. EACH CELL (i, j) REPRESENTS THE PERCENTAGE OF SAMPLES WHERE THE METHOD IN ROW i OUTPERFORMS THE METHOD IN COLUMN j IN TERMS OF F_1 -SCORE. **BOLD** VALUES HIGHLIGHT THE PERFORMANCE OF LEADER AGAINST ALL COMPETITORS.

	FingerNet	LatentAFIS	MinutiaeNet	FingerJet	FDx	VeriFinger	MINDTCT	FingerFlow	SourceAFIS	LEADER
FingerNet	—	71	100	81	63	55	72	100	91	13
LatentAFIS	28	—	100	59	34	30	54	99	82	5
MinutiaeNet	0	0	—	1	0	0	0	19	0	0
FingerJet	19	40	99	—	26	17	37	99	72	2
FDx	36	63	100	73	—	44	66	100	93	9
VeriFinger	44	68	100	80	51	—	69	100	92	7
MINDTCT	27	44	100	60	34	31	—	100	83	6
FingerFlow	0	1	80	1	0	0	0	—	1	0
SourceAFIS	9	17	100	27	7	7	15	99	—	1
LEADER (ours)	85	94	100	98	89	90	93	100	99	—

TABLE IX
PAIRWISE DIRECT-WIN RATES (%) ON NIST SD27. NOTATION AS IN TABLE VIII.

	FingerNet	LatentAFIS	MinutiaeNet	FingerJet	FDx	VeriFinger	MINDTCT	FingerFlow	SourceAFIS	LEADER
FingerNet	—	59	71	88	83	53	91	73	91	29
LatentAFIS	36	—	68	90	82	41	94	71	95	20
MinutiaeNet	26	26	—	71	57	28	82	44	83	14
FingerJet	8	7	28	—	33	7	57	31	57	2
FDx	15	15	41	64	—	12	82	45	84	3
VeriFinger	44	55	69	90	87	—	95	72	96	23
MINDTCT	5	4	16	27	13	1	—	17	38	1
FingerFlow	24	26	43	68	53	26	81	—	81	14
SourceAFIS	7	4	17	41	14	4	60	17	—	0
LEADER (ours)	64	78	83	98	96	73	99	85	100	—

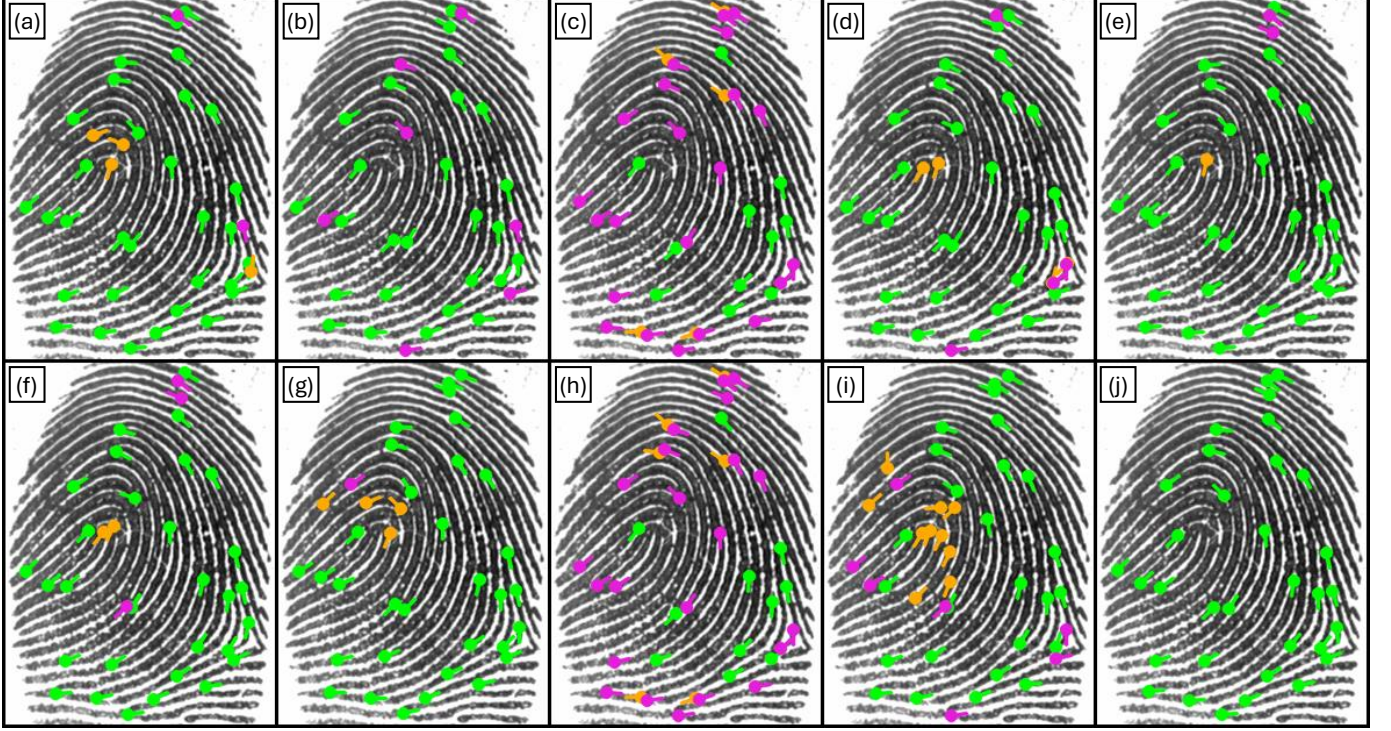


Fig. 18. **Visual comparison on an FVC2002 DB1-A sample representative of high-performance results for the proposed method.** True Positives (green), False Positives (orange), and False Negatives (magenta) are overlaid for each extractor. The metrics (TP/FP/FN/ F_1 -score) provide a sample-level performance breakdown: (a) FingerNet: 31/4/2/0.91; (b) LatentAFIS: 26/0/7/0.88; (c) MinutiaeNet: 11/5/22/0.45; (d) FingerJet: 29/4/4/0.88; (e) FDX: 31/1/2/0.95; (f) VeriFinger: 30/2/3/0.92; (g) MINDTCT: 32/4/1/0.93; (h) FingerFlow: 11/6/22/0.44; (i) SourceAFIS: 26/10/7/0.75; (j) LEADER (Ours): 33/0/0/1.0.

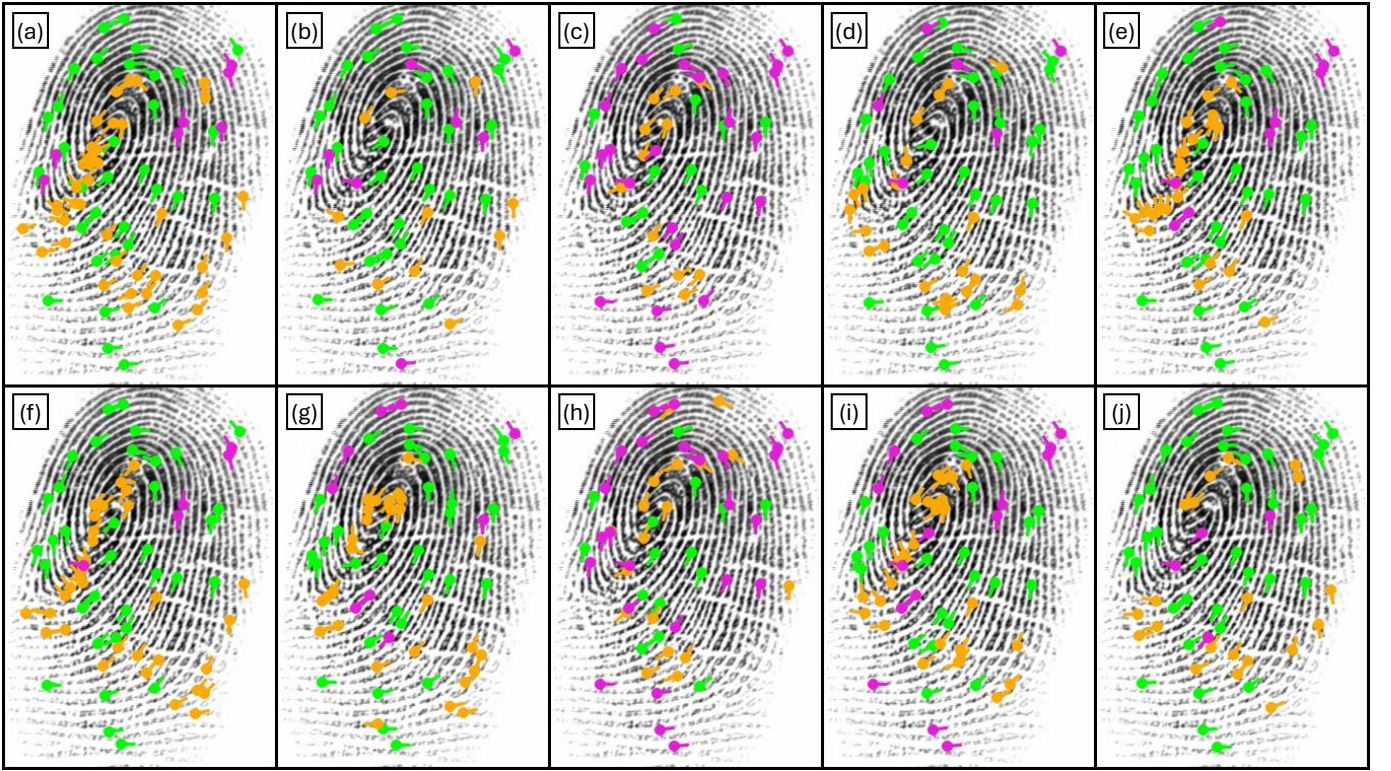


Fig. 19. **Visual comparison on an FVC2002 DB1-A sample representative of low-performance results for the proposed method.** Visual logic and metric format follow Fig. 18. (a) FingerNet: 33/39/7/0.59; (b) LatentAFIS: 32/11/8/0.77; (c) MinutiaeNet: 14/12/26/0.42; (d) FingerJet: 34/22/6/0.71; (e) FDX: 31/24/9/0.65; (f) VeriFinger: 35/32/5/0.65; (g) MINDTCT: 31/28/9/0.63; (h) FingerFlow: 15/18/25/0.41; (i) SourceAFIS: 24/28/16/0.52; (j) LEADER (Ours): 36/20/4/0.75. Note that several False Positives in this specific case are attributable to omissions in the ground truth rather than extraction failures.

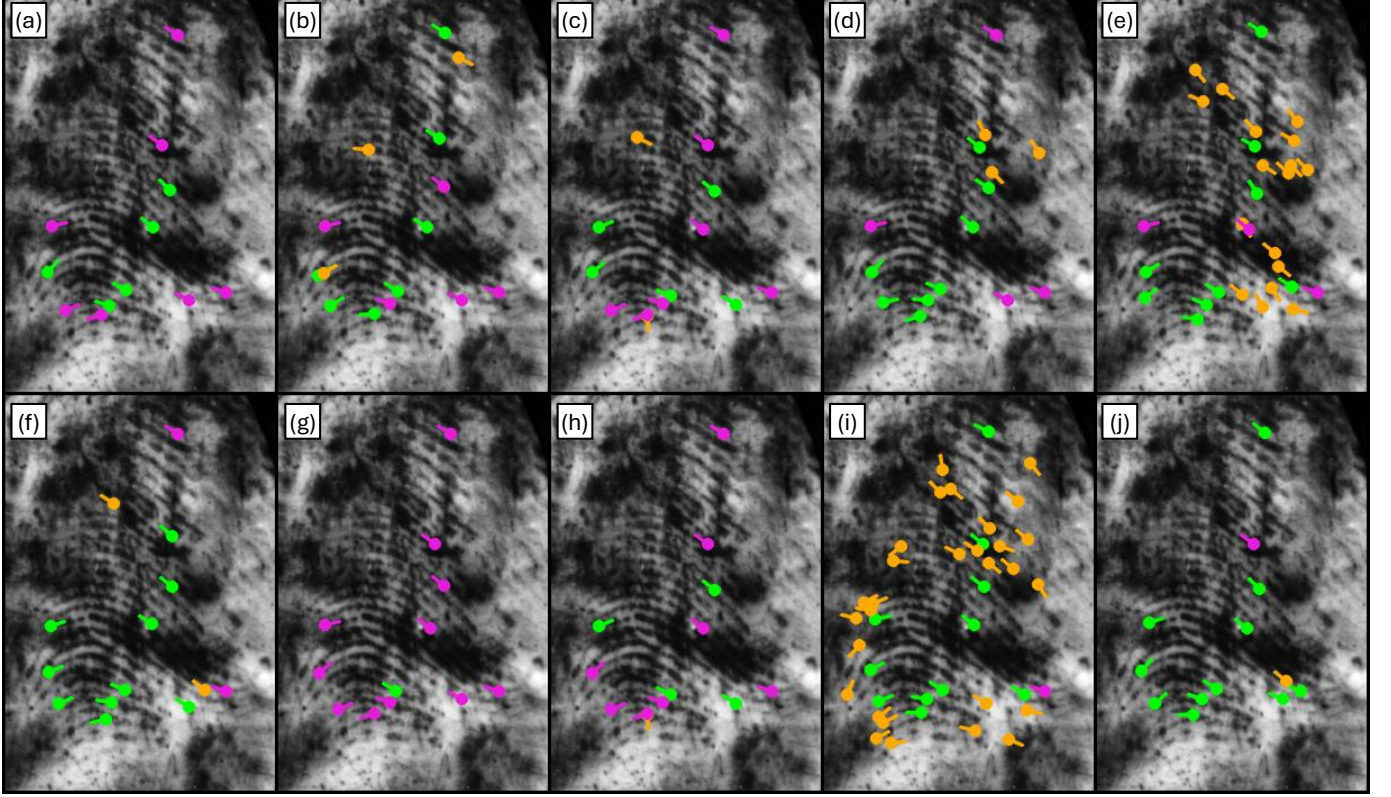


Fig. 20. **Visual comparison on a NIST SD27 latent sample representative of high-performance results for the proposed method.** Visualization logic and metric format follow Fig. 18. (a) FingerNet: 5/0/7/0.59; (b) LatentAFIS: 7/3/5/0.64; (c) MinutiaeNet: 5/2/7/0.53; (d) FingerJet: 8/3/4/0.70; (e) FDX: 9/17/3/0.47; (f) VeriFinger: 10/2/2/0.83; (g) MINDTCT: 1/0/11/0.15; (h) FingerFlow: 4/1/8/0.47; (i) SourceAFIS: 11/29/1/0.42; (j) LEADER (Ours): 11/1/1/0.92.

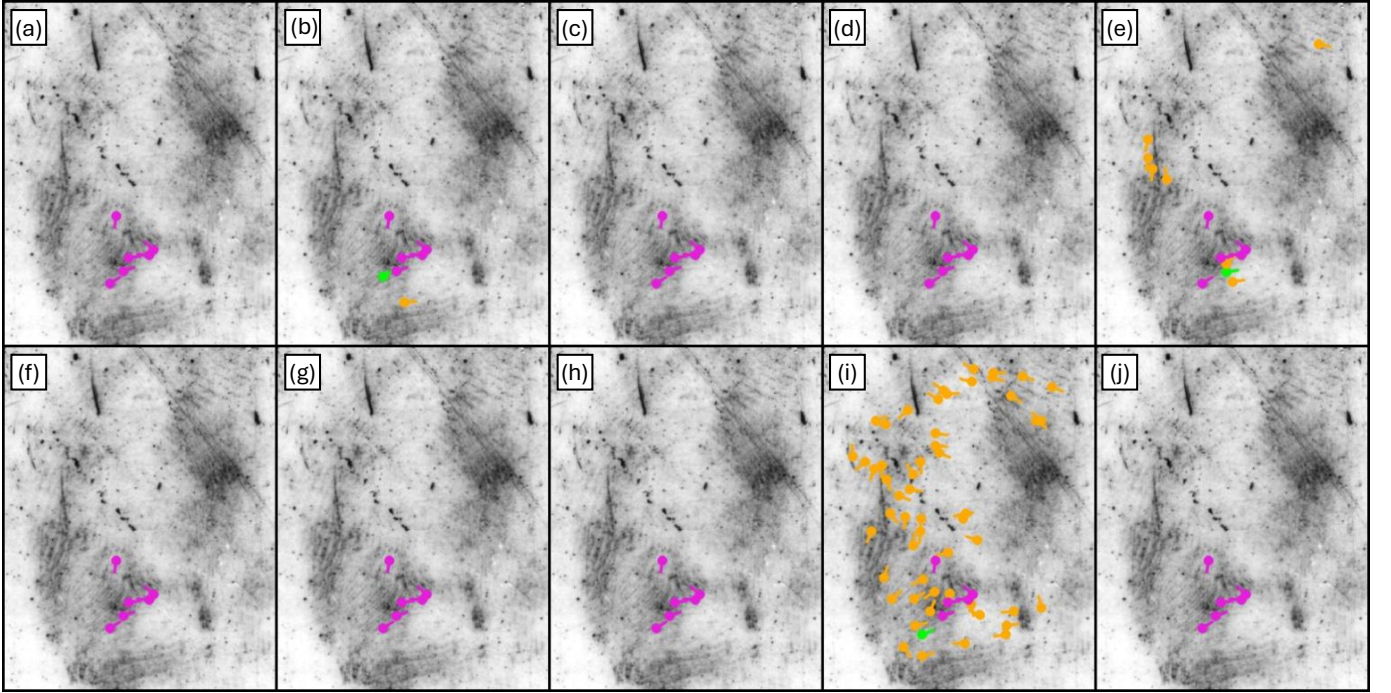


Fig. 21. **Visual comparison on a NIST SD27 latent sample representative of low-performance results for the proposed method.** Visualization logic and metric format follow Fig. 18. (a) FingerNet: 0/0/6/0.00; (b) LatentAFIS: 1/1/5/0.25; (c) MinutiaeNet: 0/0/6/0.00; (d) FingerJet: 0/0/6/0.00; (e) FDX: 1/7/5/0.14; (f) VeriFinger: 0/0/6/0.00; (g) MINDTCT: 0/0/6/0.00; (h) FingerFlow: 0/0/6/0.00; (i) SourceAFIS: 1/54/5/0.03; (j) LEADER (Ours): 0/0/6/0.00.